University of Groningen

A Multiwavelength Study of a Sample of 70 μm Selected Galaxies in the COSMOS Field

Kartaltepe, Jeyhan S.; Sanders, D. B.; Le Floc'h, E.; Frayer, D. T.; Aussel, H.; Arnouts, S.; Ilbert, O.; Salvato, M.; Scoville, N. Z.; Surace, J.

IMPORTANT NOTE: You are advised to consult the publisher's version (publisher's PDF) if you wish to cite from it. Please check the document version below.

Document Version
Publisher's PDF, also known as Version of record

[Link to publication in University of Groningen/UMCG research database](#)

A MULTIWAVELENGTH STUDY OF A SAMPLE OF 70 μm SELECTED GALAXIES IN THE COSMOS FIELD. I. SPECTRAL ENERGY DISTRIBUTIONS AND LUMINOSITIES[*]

JEYHAN S. KARTALTEPE[1,19], D. B. SANDERS[1], E. LE FLOC'H[1], D. T. FRAYER[2], H. AUSSEL[3], S. ARNOUTS[4], O. ILBERT[1,5],
M. SALVATO[6], N. Z. SCOVILLE[6], J. SURACE[7], L. YAN[7], M. BRUSA[8], P. CAPAK[6], K. CAPUTI[9], C. M. CAROLLO[9], F. CIVANO[10],
M. ELVIS[10], C. FAURE[11], G. HASINGER[8], A. M. KOEKEMOER[12], N. LEE[1], S. LILLY[9], C. T. LIU[13], H. J. MCCRACKEN[14],
E. SCHINNERER[15], V. SMOLČIĆ[6], Y. TANIGUCHI[16], D. J. THOMPSON[17], AND J. TRUMP[18]

[1] Institute for Astronomy, 2680 Woodlawn Drive, University of Hawaii, Honolulu, HI 96822, USA; jeyhan@ifa.hawaii.edu, jeyhan@noao.edu
[2] Infrared Processing and Analysis Center, California Institute of Technology 100-22, Pasadena, CA 91125, USA
[3] CNRS, AIM-Unite Mixte de Recherche CEA-CNRS-Universite Paris VII-UMR 7158, F-91191 Gif-sur-Yvette, France
[4] Canada–France–Hawaii Telescope Corporation, 65-1238 Mamalahoa Hwy, Kamuela, HI 96743, USA
[5] Laboratoire d'Astrophysique de Marseille, BP 8, Traverse du Siphon, 13376 Marseille Cedex 12, France
[6] California Institute of Technology, MC 105-24, 1200 East California Boulevard, Pasadena, CA 91125, USA
[7] Spitzer Science Center, California Institute of Technology, Pasadena, CA 91125, USA
[8] Max Planck Institut für Extraterrestrische Physik, D-85478 Garching, Germany
[9] Department of Physics, ETH Zurich, CH-8093 Zurich, Switzerland
[10] Harvard-Smithsonian Center for Astrophysics, 60 Garden Street, Cambridge, MA 02138, USA
[11] Laboratoire d'Astrophysique, Ecole Polytechnique Fédérale de Lausanne (EPFL), Observatoire de Sauverny, 1290 Versoix, Switzerland
[12] Space Telescope Science Institute, 3700 San Martin Drive, Baltimore, MD 21218, USA
[13] Astrophysical Observatory, City University of New York, College of Staten Island, 2800 Victory Blvd, Staten Island, NY 10314, USA
[14] Institut d'Astrophysique de Paris, UMR7095 CNRS, Universitè Pierre et Marie Curie, 98 bis Boulevard Arago, 75014 Paris, France
[15] Max Planck Institut für Astronomie, Königstuhl 17, Heidelberg D-69117, Germany
[16] Physics Department, Graduate School of Science, Ehime University, 2-5 Bunkyou, Matsuyama 790-8577, Japan
[17] Large Binocular Telescope Observatory, University of Arizona, 933 North Cherry Avenue, Tucson, AZ 85721-0065, USA
[18] Steward Observatory, University of Arizona, 933 North Cherry Avenue, Tucson, AZ 85721, USA
Received 2009 July 14; accepted 2009 November 25; published 2010 January 6

ABSTRACT

We present a large robust sample of 1503 reliable and unconfused 70 μm selected sources from the multiwavelength data set of the Cosmic Evolution Survey. Using the *Spitzer* IRAC and MIPS photometry, we estimate the total infrared (IR) luminosity, L_{IR} (8–1000 μm), by finding the best-fit template from several different template libraries. The long-wavelength 70 and 160 μm data allow us to obtain a reliable estimate of L_{IR}, accurate to within 0.2 and 0.05 dex, respectively. The 70 μm data point enables a significant improvement over the luminosity estimates possible with only a 24 μm detection. The full sample spans a wide range in IR luminosity, $L_{IR} \approx 10^8$–10^{14} $L_{\odot}$, with a median luminosity of $10^{11.4}$ $L_{\odot}$. We identify a total of 687 luminous, 303 ultraluminous, and 31 hyperluminous infrared galaxies (LIRGs, ULIRGs, and HyLIRGs) over the redshift range $0.01 < z < 3.5$ with a median redshift of 0.5. Presented here are the full spectral energy distributions (SEDs) for each of the sources compiled from the extensive multiwavelength data set from the ultraviolet (UV) to the far-infrared. A catalog of the general properties of the sample (including the photometry, redshifts, and L_{IR}) is included with this paper. We find that the overall shape of the SED and trends with L_{IR} (e.g., IR color temperatures and optical–IR ratios) are similar to what has been seen in studies of local objects; however, our large sample allows us to see the extreme spread in UV to near-infrared colors spanning nearly 3 orders of magnitude. In addition, using SED fits we find possible evidence for a subset of cooler ultraluminous objects than observed locally. However, until direct observations at longer wavelengths are obtained, the peak of emission and the dust temperature cannot be well constrained. We use these SEDs, along with the deep radio and X-ray coverage of the field, to identify a large sample of candidate active galactic nuclei (AGNs). We find that the fraction of AGNs increases strongly with L_{IR}, as it does in the local universe, and that nearly 70% of ULIRGs and all HyLIRGs likely host a powerful AGN.

Key words: cosmology: observations – galaxies: active – galaxies: evolution – galaxies: high-redshift – infrared: galaxies – surveys

Online-only material: color figures, machine-readable table

1. INTRODUCTION

Luminous and ultraluminous infrared galaxies (LIRGs, $L_{IR} = 10^{11}$–10^{12} $L_{\odot}$, and ULIRGs, $L_{IR} = 10^{12}$–10^{13} $L_{\odot}$) have played a major role in the study of galaxy formation and evolution since their initial discovery. They were first identified in large

numbers in the local universe by the *Infrared Astronomical Satellite* (*IRAS*) and follow-up redshift surveys revealed that though they are rare in the local universe, their number density increases strongly with redshift (e.g., the Bright Galaxy Survey (BGS): Soifer et al. 1989; the Revised Bright Galaxy Survey (RBGS): Sanders et al. 2003; 1 Jy ULIRG Survey: Kim & Sanders 1998).

Since the launch of the *Spitzer Space Telescope*, many deep infrared surveys (particularly at 24 μm where the MIPS detector is most sensitive) have been undertaken and have shaped our view of the significance of IR galaxies out to $z \sim 1$. We now know that the cosmic star formation rate is dominated by LIRGs beyond $z > 0.7$ (Le Floc'h et al. 2005) and ULIRGs start to dominate by $z \sim 2$ (Caputi et al. 2007; Magnelli et al. 2009). However, one limitation in all 24 μm selected studies is the difficulty in obtaining an accurate and reliable measurement of the total infrared luminosity of these sources since the 24 μm selection wavelength represents rest-frame 12 μm by $z = 1$ and 8 μm by $z = 2$. Since the peak of the infrared emission for star-forming galaxies and galaxies with active galactic nuclei (AGNs) is typically at $\sim$50–200 μm, at higher redshifts the selection wavelength moves further from the peak and becomes heavily influenced by the presence of polycyclic aromatic hydrocarbon (PAH) features.

In order to study how various galaxy properties are related to luminosity, an accurate estimate of the total infrared luminosity is needed. Previous studies (Bavouzet et al. 2008; Symeonidis et al. 2008) have shown that rest-frame monochromatic luminosities in the mid-infrared (MIR) correlate very well with the total $L_{\rm IR}$, but they show a considerable amount of scatter. Of course, this problem becomes worse at higher redshifts as observed MIR probes shorter wavelengths. Ideally, one would use observations in the far-infrared (FIR) and submillimeter in order to sample the peak of the infrared emission in these sources, but current IR and submillimeter detectors lack the sensitivity to reach the necessary depths and only the most luminous sources are detected. Studies at long wavelengths are also hampered by confusion due to the large beam size of most detectors.

Previous studies (e.g., Huynh et al. 2007; Symeonidis et al. 2008; Magnelli et al. 2009) based on 70 μm selected sources have been hampered by this sensitivity problem and have lacked the depth or area necessary to detect a large sample of objects over a wide range of luminosities and redshifts. Deep surveys over small areas allow the detection of fainter, lower-luminosity sources, but they suffer from cosmic variance and poor statistics. Shallow surveys over wide areas only sample the bright end of the luminosity function. In order to overcome these problems, we have obtained deep imaging at 24, 70, and 160 μm over the entire $\sim$2 deg^2 of the Cosmic Evolution Survey (COSMOS) field (Le Floc'h et al. 2009; Frayer et al. 2009).

COSMOS (Scoville et al. 2007b) was designed to study galaxy evolution over a large range of redshifts and environments, particularly with respect to large-scale structure. The initial *Hubble Space Telescope* (*HST*) imaging (Koekemoer et al. 2007) has been complemented with wide multiwavelength coverage from space and the ground. Along with many spectroscopic redshifts, the deep multiwavelength photometry has allowed us to obtain photometric redshifts with unprecedented accuracy, both for normal galaxies (Ilbert et al. 2009) and AGNs (Salvato et al. 2009). This unique data set provides the first opportunity to study the properties of a large sample of 70 μm selected sources in detail over a wide range in redshift, luminosity, and environment.

This paper is the first of a two-part series on the properties of a large sample of $\sim$1500 70 μm selected galaxies in the COSMOS field. Section 2 summarizes the COSMOS data sets used for this study, and our sample selection is described in Section 3 along with a summary of general properties of the sources. We present the full ultraviolet (UV)–FIR spectral energy distributions (SEDs) and describe the estimate of their total infrared luminosity in Section 4. We discuss our results and their implications in Section 5 and present our conclusions in Section 6. Paper II will discuss the morphological and optical color properties of these sources as a function of redshift and luminosity. Throughout this paper, we assume a ΛCDM cosmology with $H_0 = 70 \, {\rm km \, s^{-1} \, Mpc^{-1}}$, $\Omega_\Lambda = 0.7$, and $\Omega_m = 0.3$. All magnitudes are in the AB system unless otherwise stated.

2. THE DATA SETS

The imaging data used for this study were obtained as part of the *HST*-COSMOS project (Scoville et al. 2007a). COSMOS originated as an *HST* treasury program imaging a $\sim$2 deg^2 equatorial field with the Advanced Camera for Surveys (ACS), using the $F814W$ filter (*I* band). This is the largest contiguous field ever observed by *HST*. To supplement the ACS coverage, follow-up observations have been obtained across the entire spectrum using both space- and ground-based facilities. A complete description of the COSMOS data sets can be found in Scoville et al. (2007b). In this section, we provide a brief description of each data set and refer the reader to the relevant papers. These data sets are summarized in Table 1.

2.1. S-COSMOS

Spitzer-COSMOS (S-COSMOS; Sanders et al. 2007) is a *Spitzer* legacy survey designed to cover the entire 2 deg^2 COSMOS field with both the MIPS and IRAC instruments. The deep IRAC data for the full COSMOS field was taken during cycle 2 (2006 Jan) with a total of 166 hr to cover the field in all four bands (3.6, 4.5, 5.6, and 8 μm) down to a total depth of 1200 s. The 5σ sensitivity at 3.6 μm is 0.9 μJy. For a detailed description of the data reduction of all S-COSMOS data, see Sanders et al. (2007).

The MIPS coverage of the COSMOS field was taken during cycles 2 and 3. The aim of the cycle 2 observations was to obtain shallow (80, 40, and 8 s per pixel at 24, 70, and 160 μm, respectively) imaging over a large $\sim$4 deg^2 area centered on the COSMOS field. In addition to the shallow imaging, deeper imaging was obtained for a small test region covering $\sim$8% of the field. The total depths obtained over this test region were 3200, 1560, and 320 s at 24, 70, and 160 μm, respectively, with a 5σ sensitivity of 0.071, 7.5, and 70 mJy. Deep MIPS imaging was obtained for the entire field during cycle 3 (2007 Jan–May and 2008 Jan) with a depth of 3400, 1350, and 273 s at 24, 70, and 160 μm with a 5σ sensitivity of 0.08, 8.5, and 65 mJy, respectively.

The cycles 2 and 3 MIPS 24 μm data were combined and reduced using the MOPEX package (Makovoz & Khan 2005) to produce a final mosaic. The source catalog was produced using SExtractor (Bertin & Arnouts 1996) for source detection and the DAOPHOT package (Stetson 1987) for measuring flux densities using the point-spread function (PSF) fitting technique. This final catalog is >90% complete above 80 μJy and $\sim$80% complete above 60 μJy. Details on the 24 μm observations, data reduction, and source properties are presented in Le Floc'h et al. (2009).

Table 1
Summary of COSMOS Multiwavelength Data Sets

Instrument	Band	Date of Observations	Depth (5σ)	No. in 70 μm Sample
Spitzer/IRAC	3.6 μm	2006	0.9 μJy	1503
Spitzer/IRAC	4.5 μm	2006	1.7 μJy	1503
Spitzer/IRAC	5.6 μm	2006	11.3 μJy	1501
Spitzer/IRAC	8.0 μm	2006	14.6 μJy	1503
Spitzer/MIPS	24 μm	2006–2008	80 μJy	1503
Spitzer/MIPS	70 μm	2006–2008	8.5 mJy	1503
Spitzer/MIPS	160 μm	2006–2008	65 mJy	463
HST/ACS	$F814W$	2003–2005	27.2 mag	1503
HST/NICMOS	$F160W$	2003–2005	25.9 mag	74
GALEX	FUV, NUV	2004	25.7, 26.0 mag	892, 1284
XMM-Newton	0.5–10 keV	2004–2005	$5 \times 10^{-16}\,\mathrm{erg\,cm^{-2}\,s^{-1}}$	119
Chandra	0.5–10 keV	2006–2007	$5.7 \times 10^{-16}\,\mathrm{erg\,cm^{-2}\,s^{-1}}$	103
CFHT/MEGACAM	u^*	2003–2007	26.5 mag	1502
Subaru/SuprimeCam	$B_J V_J g^+ r^+ i^+ z^+$	2004–2005	$i^+ \sim 26.2$ mag	1503
UKIRT/WFCAM	J	2004–2007	23.7 mag	1498
CFHT/WIRCAM	K_S	2005–2007	23.5 mag	1503
VLA	1.4 GHz	2003–2005	55 μJy	562

The raw 70 and 160 μm data were reduced using the Germanium Reprocessing Tools (GeRT) and then combined using the MOPEX package. The source detection was done using the Astronomical Point-Source Extraction (APEX) tools within MOPEX. The systematic photometric errors are 5% and 12% at 70 and 160 μm, respectively. Details on the 70 and 160 μm observations, data reduction, catalogs, and source counts are presented in Frayer et al. (2009).

2.2. Hubble Space Telescope Images

The *HST*/ACS images were taken during *HST* cycles 12 and 13 as part of the COSMOS treasury survey. A total of 583 orbits were used to obtain a coverage of 1.64 deg^2 in the $F814W$ filter. The ACS images were taken between 2003 October and 2005 June and reach a depth of 27.2 mag (5σ). Details of the ACS images, including their calibration and reduction, are given in Koekemoer et al. (2007). In addition to the ACS images, NICMOS parallel images were taken over $\sim$6% of the ACS area in the $F160W$ (*H* band) filter down to a depth of 25.9 mag (5σ). The high resolution of the ACS images (FWHM = 0''.09) is necessary for the detailed morphological analysis presented in Paper II. The NICMOS parallel images (FWHM = 0''.16) are particularly useful for studying the effects of morphological *k*-corrections. Due to the requirement of morphological information for this study, we limited our sample to sources within the ACS area.

2.3. Ground-based UV/Optical/NIR Data

The ground-based UV, optical, and near-infrared (NIR) coverage consists of data taken with Subaru–SuprimeCam (B_J, V_J, g^+, r^+, i^+, z^+), CFHT–Megacam (u^*, i^*), UKIRT–WFCAM (J), and CFHT–WIRCAM (K_S). The complete description of the data reduction of the optical and NIR ground-based data can be found in P. Capak et al. (2010, in preparation).

The broadband optical data (B_J, V_J, g^+, r^+, i^+, z^+) were taken in 2004–2005 using SuprimeCam on the 8 m Subaru Telescope on Mauna Kea in Hawaii. The seeing ranged from 0''.4 to 2''.0 and the depth at i^+ is 26.2 mag. Deep u^* and i^* images were obtained using the Megacam camera at the 3.6 m Canada–France–Hawaii Telescope (CFHT) with a depth of 26.5 mag at u^*.

The *J* band images were taken in several observing runs between 2004 and 2007 with the Wide-field Camera on the 3.8 m United Kingdom Infrared Telescope (UKIRT) and the K_S band images were taken in queue mode between 2005 and 2007 with the Wide-field Infrared Camera (WIRCAM) at CFHT. The data were reduced using custom scripts in IRAF.[20] The TERAPIX software Scamp (Bertin 2006) was used to calculate the astrometric solution and the final images were combined using Swarp (Bertin et al. 2002). The final catalogs are complete to $J = 23.7$ and $K_S = 23.5$ mag. For details on the reduction of the K_S images, see McCracken et al. (2009).

Photometry for all of these data sets was produced using SExtractor in dual mode (Bertin & Arnouts 1996) using the *I*-band image as the detection image and have been combined into a master catalog.

2.4. GALEX UV Data

UV data were taken using the *Galaxy Evolution Explorer* (*GALEX*) in 2004. Four pointings of 50 ks each were used to observe the entire COSMOS field (Zamojski et al. 2007) in the near- and far-ultraviolet bands (NUV and FUV). The u^* images from CFHT were used as a prior for the flux measurements of the *GALEX* images. These data reach a limiting magnitude of 25.7 and 26.0 in the FUV and NUV, respectively.

2.5. X-ray Data

The COSMOS field was observed with the *XMM-Newton* satellite in 2004–2005 for a total of $\sim$1.5 Ms (Hasinger et al. 2007). A total of 1887 point sources were detected in at least one of the bands (soft: 0.5–2 keV, hard: 2–10 keV, and ultrahard: 5–10 keV). The limiting fluxes in each of these bands are 5×10^{-16}, 2×10^{-15}, and 5×10^{-15} erg cm^{-2} s^{-1} for the soft, hard, and ultrahard bands, respectively (Cappelluti et al. 2009). The *Chandra*-COSMOS survey (C-COSMOS) observed the central 0.5 deg^2 of the COSMOS field to a depth of 160 ks and an outer 0.4 deg^2 to a depth of 80 ks with the *Chandra X-ray Observatory* (Elvis et al. 2009). The flux limits obtained are 1.9×10^{-16} and 7.3×10^{-16} erg cm^{-2} s^{-1} for the soft (0.5–2 keV) and hard (2–10 keV) bands, respectively. A total of 1761 point sources have been detected and are presented in the

[20] http://iraf.noao.edu/

Table 2
Spectroscopic Redshift Surveys

Survey	Reference	Instrument	Wavelength Range (Å)	No. in 70 μm Sample
24 μm sources	J. S. Kartaltepe et al., 2010, in preparation	Keck II/DEIMOS	4000–10000	62
...	P. Capak & M. Salvato et al., 2010, in preparation	Keck II/DEIMOS	4000–10000	18
zCOSMOS	Lilly et al. 2007	VLT/VIMOS	5550–9650	355
XMM-Newton sources	Trump et al. 2007, 2009	Magellan/IMACS	5600–9200	223
Quasar candidates	Prescott et al. 2006	MMT/Hectospec	3100–9000	43
...	Anguita et al. 2009	VLT/FORS1	3300–11000	4
SDSS	Abazajian et al. 2009	SDSS Spectrograph	3900–9100	65
2dFGRS	Colless et al. 2001	2dF Spectrograph	3500–10000	34

catalog of Elvis et al. (2009). In this paper, we use the optical identification catalogs (Brusa et al. 2009; F. Civano et al. 2010, in preparation) from both of these data sets to identify AGNs among our 70 μm selected sample of galaxies.

2.6. Radio Data

The COSMOS field was observed with the Very Large Array (VLA) at 1.4 GHz as part of a VLA Large Project in 2004–2005 for a total of 280 hr in A and C configurations to cover the entire 2 deg^2 (Schinnerer et al. 2007). The data have a mean rms noise of 10.5 μJy beam^{-1} and a 5σ sensitivity of 55 μJy. The catalog used here consists of ∼2417 sources with signal-to-noise ratio (S/N) > 5 (Bondi et al. 2008).

2.7. Spectroscopy

Spectra of the 70 μm sources were obtained from several different sources. The first is a follow-up survey of 24 μm sources in the deep MIPS test region of the field using DEIMOS on Keck II. The complete survey details will be described in J. S. Kartaltepe et al. (2010, in preparation). The observations were taken on five nights between 2007 and 2009 using the 600 l mm^{-1} grating with a 1″ wide slit and typical slit lengths of ∼6″. The typical wavelength coverage with these settings is 4000–10,000 Å with a dispersion of 0.65 Å per pixel and a spectral resolution of 4.6 Å. The total integration times were between 1 and 3 hr, depending on the magnitudes of the sources. The data were reduced using the DEEP2 pipeline[21] and redshifts were measured individually for each source and a quality flag 1–4 was assigned, with 4 being a very secure redshift based on multiple lines, 3 being a likely redshift based on multiple lines, 2 being a less reliable redshift often based on only one line and a noisy spectrum, and 1 being a best-guess redshift based on a noisy spectrum. A total of 62 70 μm detected sources have DEIMOS spectroscopy.

Spectra were also drawn from the zCOSMOS-bright 10k sample (Lilly et al. 2007) observed with the Visible Multi-Object Spectrograph (VIMOS; Le Fèvre et al. 2003) on the 8 m Very Large Telescope (VLT) in Paranal, Chile. This sample consists of the first 10,000 galaxies from a large flux-limited ($I < 22.5$) survey of galaxies over the entire COSMOS field. The zCOSMOS-bright survey used the $R \sim 600$ MR grism with a velocity resolution of <100 km s^{-1} and a wavelength range of 5550–9650 Å.

Additional spectra have been obtained from a survey of 677 *XMM-Newton* selected AGN candidates with the Inamori Magellan Areal Camera and Spectrograph (IMACS) on the 6.5 m Magellan (Baade) Telescope from 2005 to 2008 on a total of 18 clear nights (Trump et al. 2007, 2009). The 200

and 150 l mm^{-1} gratings were used. The wavelength range of these spectra is 5600–9200 Å with a resolution of 10 Å for the lower resolution 150 l mm^{-1} grating. While AGNs were the main targets of this survey, additional sources were observed when possible. Similarly, Prescott et al. (2006) conducted a spectroscopic survey of quasar candidates using the Hectospec multiobject spectrograph on the 6.5 m MMT on Mount Hopkins using the 270 l mm^{-1} grating and covering a wavelength range of 3100–9000 Å. Four sources were also observed using the Focal Reducer and low dispersion Spectrograph (FORS1) on the VLT (PI: C. Faure) covering a wavelength range of 3300–11,000 Å (Anguita et al. 2009).

In addition to the surveys described above, spectra of the 70 μm sources were found on the NASA Extragalactic Database (NED) public archive from the Sloan Digital Sky Survey (SDSS; Abazajian et al. 2009) and the Two-degree Field Galaxy Redshift Survey (2dFGRS; Colless et al. 2001). See Table 2 for a summary of the spectroscopic surveys and a breakdown of the number of sources that were observed by each.

3. THE 70 μm SAMPLE

We restricted our study to the area of the field with *HST*/ACS coverage and selected sources at 70 μm with S/N > 3. After removing spurious sources detected around bright objects and removing sources in areas around bright stars masked out in the optical or IRAC photometry, the number of sources remaining is 1743. These 1743 sources represent the initial catalog of 70 μm selected sources discussed below. This catalog includes sources within the deeper cycle 2 MIPS coverage area as well as the full field cycle 3 coverage, therefore, the deeper area has a slightly lower flux limit (∼5 mJy). The distribution of 70 μm fluxes for the deep area and the rest of the field is shown in Figure 1.

3.1. Identification of Counterparts

In order to ensure the most reliable identification of the optical counterpart for each source in our sample, we first matched the cleaned 70 μm catalog to the 24 μm catalog. Figure 2 shows the separation between the 70 μm source positions and the nearest (as well as the second and third nearest) 24 μm source. Seventy nine of the 70 μm sources (4.5%) do not have a 24 μm counterpart within the 18″ 70 μm beam or there is one on the very edge that does not appear to be a likely counterpart. The vast majority of these sources (92%) are at the low S/N end (3 < S/N < 4). In order to be not detected at 24 μm, these sources would have to have a 70 to 24 μm flux ratio of > 100. Sources with this extreme flux ratio are very rare in the rest of the sample with 24 μm counterparts (at the 1% level). Physically, such a large flux ratio is possible at $z > 2$ where 24 μm could potentially pass through a silicate absorption feature at rest-frame 8 μm; however, given the large number of sources not
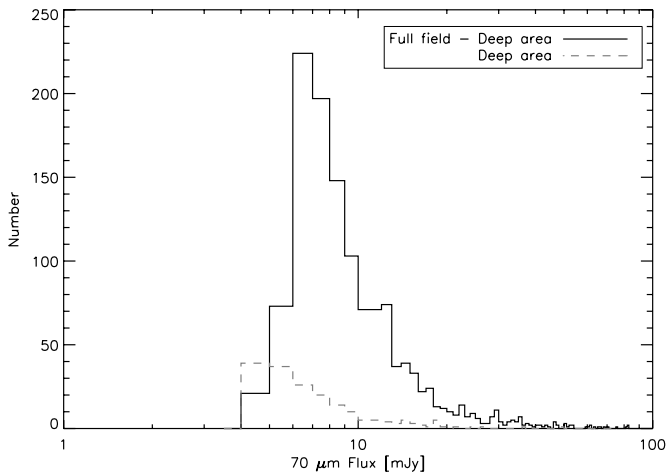
**Figure 1.** Histogram of 70 μm source fluxes in the deep MIPS test area (covering $\sim$0.16 deg^2: gray dashed) and the full COSMOS field (covering 1.64 deg^2) excluding the deep area (black). The test area represents $\sim$9% of the COSMOS field and contains $\sim$ 12% of the 70 μm sources (includes more sources since this region is deeper). The flux limit for the full field is $\sim$6.5 mJy and the flux limit for the deep area is $\sim$ 5 mJy for sources with S/N > 3.

detected it is unlikely that all of them are such extreme high-redshift sources. Furthermore, there are no sources in the local universe with such extreme ratios between rest-frame 8 and 24 μm. This, combined with their low S/N, indicates that they are most likely spurious detections and we therefore remove them from further analysis.

Of the remaining 1664, 1528 sources were successfully matched to a 24 μm counterpart. Of the 1528 successfully matched sources, 759 ($\sim$50%) have a single isolated 24 μm source within the 70 μm beam making the identification of the correct counterpart straightforward. For 513 sources ($\sim$34%) there is more than one 24 μm source in the beam but the most likely counterpart is clear (i.e., the source closest to the center of the beam is also the brightest at 24 μm). Two hundred and fifty six sources ($\sim$17%) have more than one 24 μm source in the beam but the likely counterpart is not as clear as in the previous case. For these sources we chose the source with the highest 24 μm flux as the best-guess match to the counterpart. Although it is possible that some fraction of these "best-guess" matches are the wrong counterpart, we find that the results of our analysis do not change if they are left out. We estimate that our false match rate is on the order of 2.5%. For the 136 sources that cannot be matched, there either appears to be more than one equally likely counterpart or the 70 μm source appears to be a blend of multiple 24 μm sources. It is highly probable that the multiple 24 μm sources within the beam each contribute to the 70 μm flux, and therefore it is not possible to determine an accurate 70 μm flux for each source. Leaving these sources in our sample will only add an additional uncertainty, therefore we omit these ambiguous sources from further discussion.

We then matched the remaining 1528 sources with believable 24 μm counterparts to the IRAC source positions. All but nine of them have a clear match within 2″ of the 24 μm source position. For these nine, the 24 μm source appears to be a blend of two IRAC sources so we remove them from the sample for the same reasons described above. For the remaining 1520 sources, we then matched the IRAC counterparts to the optical I-band positions and found clear counterparts for all but 11. Five of these appear to be two optical sources with blended IRAC photometry, so we also exclude these five sources from our sample. The remaining six sources (0.3%) do not have an
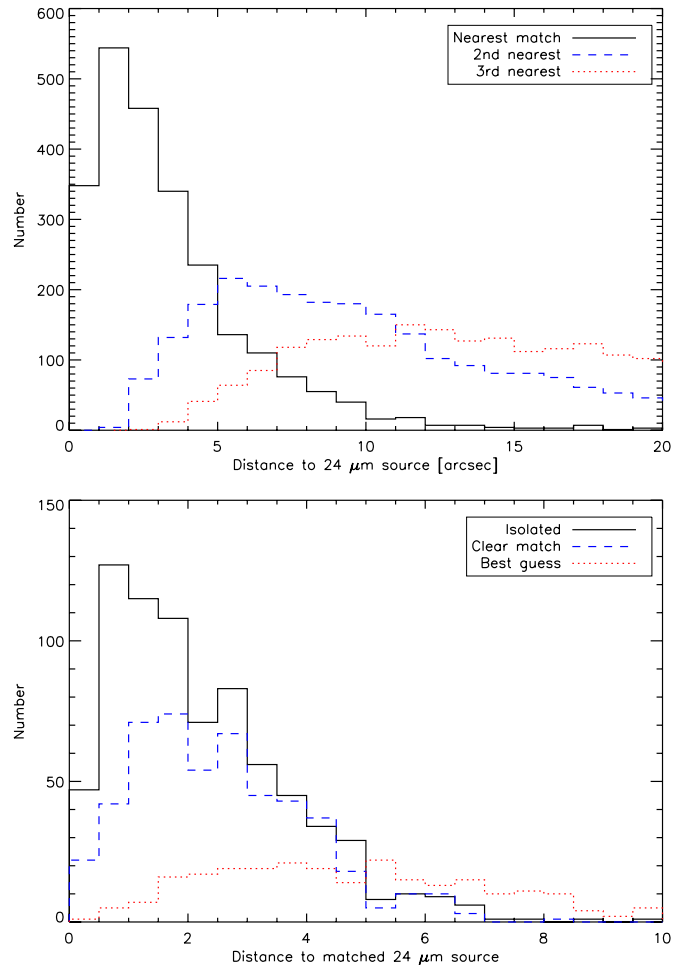

Figure 2. Top: angular separation between each 70 μm source position and the nearest (as well as the second and third nearest) 24 μm source. Bottom: separation between matched source 70 and 24 μm positions for the three different cases—those that are isolated (black), those that have a clear match (blue dashed), and those with a best-guess match (red dotted).

(A color version of this figure is available in the online journal.)

optical counterpart above the flux limit of the catalog. Without an optical counterpart we have no redshift measurement for these six sources and thus cannot obtain an estimate of the total infrared luminosity, so we exclude them from our final sample but note that their IRAC/MIPS properties do not appear to differ from the rest of the sample. Of the remaining 1508 sources, five are stars and so we remove them from the final sample as well. This results in a final sample size of 1503 70 μm selected sources with reliable counterparts at 24 μm, the IRAC bands, and the optical. We believe that the 9% of the sources removed from our sample (136 + 9 + 11) due to their inability to be matched will not affect our final result and removing them leaves us with a robust sample.

We plot the differential source counts ($dN/dS \times S^{2.5}$) for the final sample of 1503 sources in Figure 3 along with the published source counts from S-COSMOS (Frayer et al. 2009) and GOODS-N (Frayer et al. 2006). The source counts for our sample match the published source counts very well except at the lowest flux bin ($S70 < 6.5\ \mu$Jy). This indicates that spurious sources at low S/N do not have a significant contribution and that the sample is therefore reliable though incomplete at these low flux levels.

The cross matching at 160 μm was done by looking for 160 μm sources near each of the 70 μm sources. For the
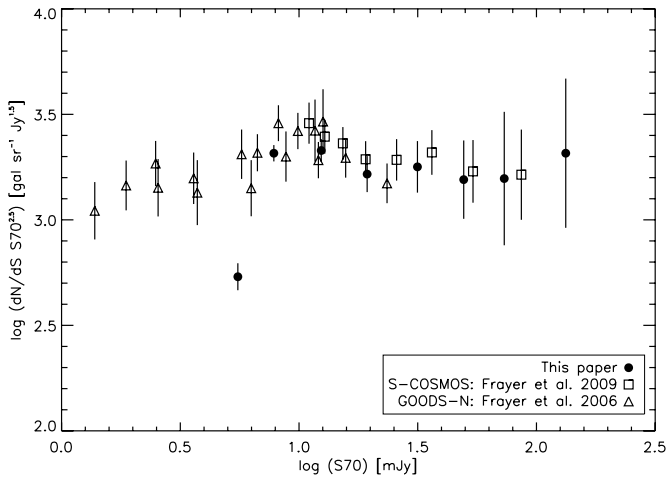
Figure 3. Differential source counts ($dN/dS \times S^{2.5}$) for the final sample of 1503 sources compared to the published S-COSMOS (Frayer et al. 2009) and GOODS-N (Frayer et al. 2006) source counts. Note that the counts agree except at the lowest flux bin ($S70 < 6.5$ μJy).

vast majority of the cases (89%), only one 70 μm source was identified as a possible match to a 160 μm source. For most of the cases where more than one 70 μm source could have been identified as a possible match, one was much closer to the center of the beam and the other was far enough away that the choice was unambiguous (9%). For the handful of ambiguous cases (remaining 2%), we chose the brighter 70 μm source as the match. In total, we find that 463 of the 1503 70 μm selected sources ($\sim$31%) are detected at 160 μm.
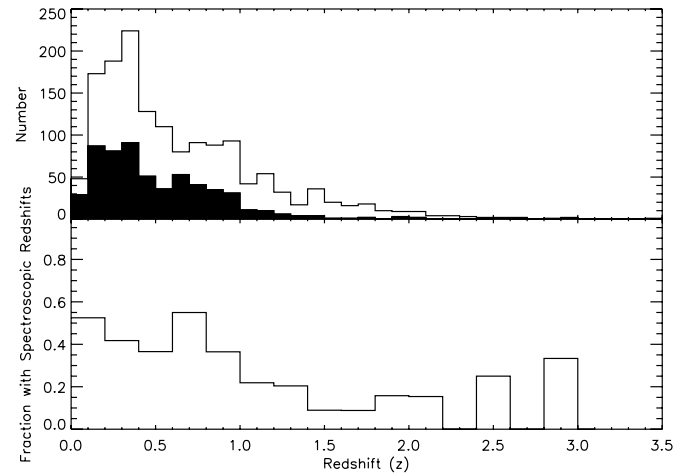
3.2. Photometric Redshifts

All of the UV–NIR (including *GALEX*, IRAC, and all of the ground-based optical and NIR) multiwavelength photometry was used to produce a photometric redshift catalog for all galaxies (Ilbert et al. 2009) and X-ray detected AGNs (Salvato et al. 2009) in the COSMOS field. Thanks to the depth and broad range of this multiwavelength coverage, the COS-MOS photometric redshifts have an unprecedented accuracy of $dz/(1 + z) = 0.007$ at $i^+ < 22.5$ and 0.012 at $i^+ < 24$ out to $z < 1.25$. The AGN photometric redshifts have an accuracy of $dz/(1 + z) = 0.02$ and 0.03 for $i^+ < 22.5$ and $22.5 < i^+ < 25$, respectively. The number of outliers for both galaxies and AGNs are negligible. The accuracy and high precision of these photometric redshifts allows us to use our entire sample for the analysis of the properties of 70 μm sources instead of limiting our sample to those with spectroscopy as has generally been done in the past.

The redshift distribution of the entire 70 μm sample is shown in Figure 4. Photometric redshifts are available for all of the 1503 galaxies in the sample. One hundred and fifty four of these sources are detected in the X-ray by *XMM-Newton* and *Chandra*, and so we use the photometric redshifts determined by Salvato et al. (2009). Our 70 μm selected sample peaks at $z \sim 0.35$ and the number of sources drops beyond ($z \sim 1$). However, given our large sample size, a significant number (273: 18%) are detected at $1 < z < 3$.

3.3. Spectroscopic Redshifts

Reliable spectroscopic redshifts are available for 602 sources in the sample ($\sim$40%) and are represented by the filled histogram in Figure 4. Column 5 in Table 2 lists the number of sources in our sample that have spectra from each of the different


Figure 4. Top: redshift distribution of the entire 70 μm selected sample (white: photometric redshifts) and those with spectroscopy (black). Bottom: fraction of sample with reliable spectroscopic redshifts as a function of redshift. Note that spectroscopic redshifts are available for $\sim$40% of the sample and spread across the entire redshift range.
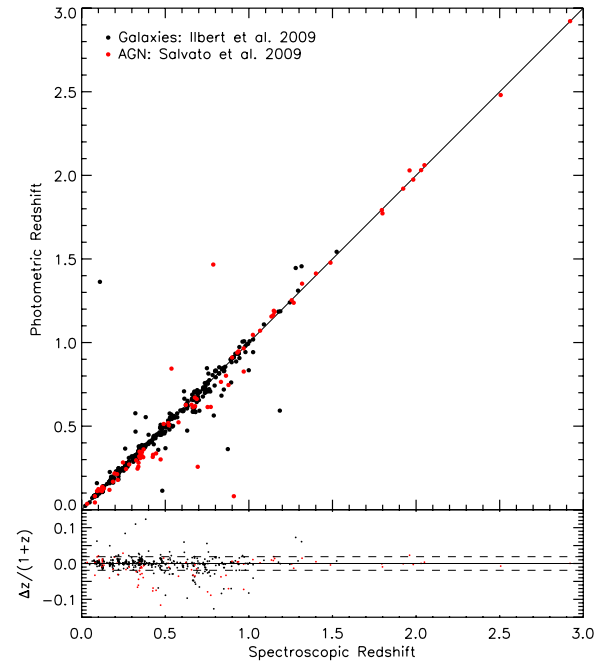
Figure 5. Comparison of photometric and spectroscopic redshifts. Photometric redshifts are from Ilbert et al. (2009, for normal galaxies) and Salvato et al. (2009, for X-ray detected AGNs marked with red boxes). Note that the agreement is excellent for the AGNs as well as the normal galaxies. The overall dispersion is $0.02 \times (1 + z)$ (shown as dashed lines in the bottom panel) and the fraction of catastrophic failures is 1.7%.

(A color version of this figure is available in the online journal.)

redshift surveys. Several sources have redshifts available from more than one source. For these objects, we compared each available redshift to check their reliability and chose the best one. A comparison between the photometric and spectroscopic redshifts for those sources with very secure redshifts (quality flags 3 and 4) is shown in Figure 5. The *XMM-Newton* sources are shown as the red points and use the photometric redshifts of Salvato et al. (2009). The overall dispersion in this infrared selected sample is $0.02 \times (1 + z)$. There are only nine catastrophic failures ($|z_p - z_s|/(1 + z_s) > 0.15$) in the sample (1.7%). For the rest of the paper, we adopt the spectroscopic redshift for those
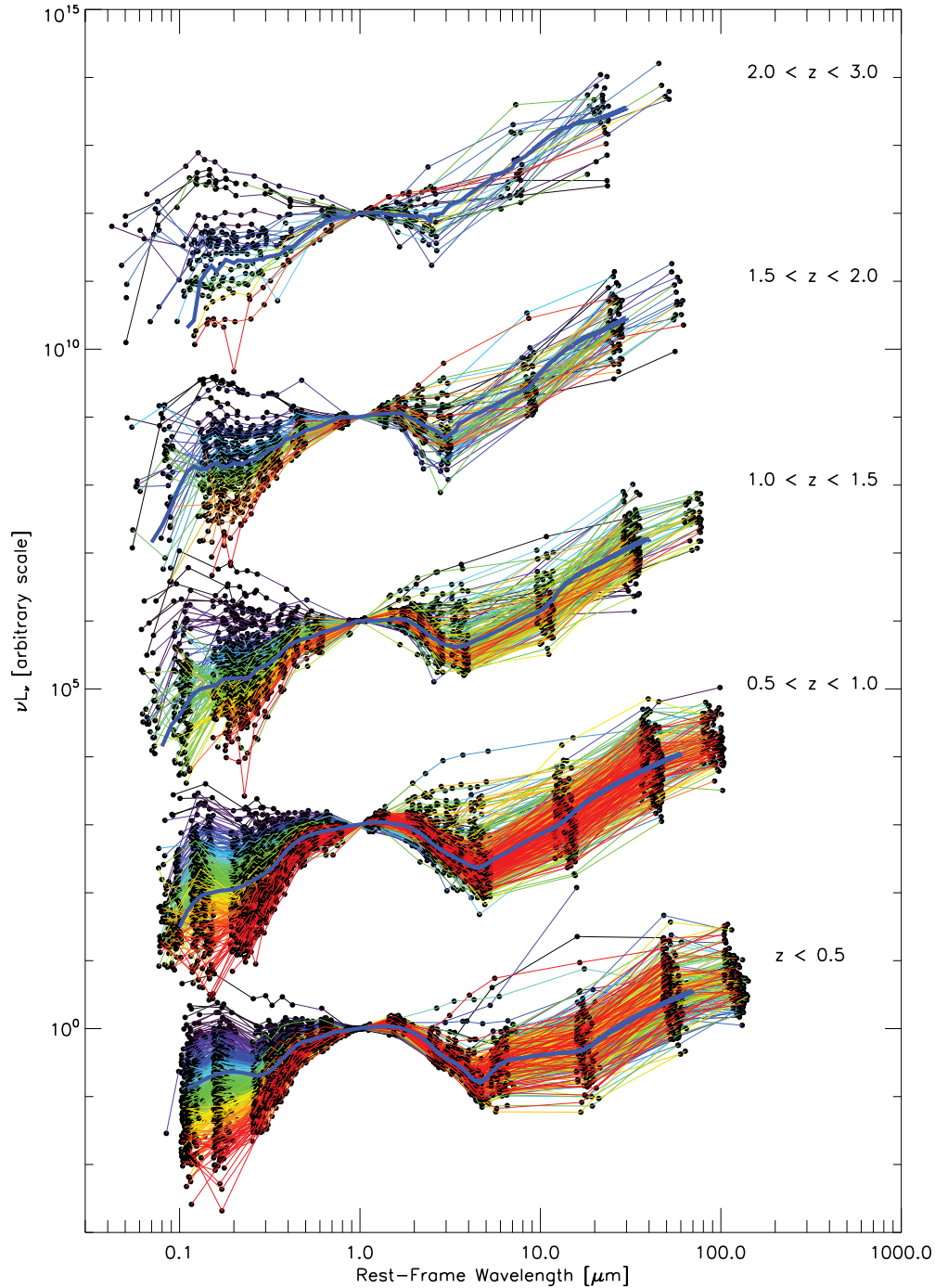
Figure 6. SEDs of all 1503 70 μm sources binned by redshift and normalized at 1 μm. The SEDs are color coded such that the ones with the bluest slope in the UV–optical are purple/blue and the reddest are red and the spectrum in between shows the range of SED colors. The median SED for each bin is overplotted in blue. Note that at higher redshifts the SEDs extend further into the UV, while the FIR points probe shorter wavelengths.

(A color version of this figure is available in the online journal.)

sources with reliable spectroscopy and the photometric redshift for the rest of the sample.

3.4. UV-to-FIR Spectral Energy Distributions

Figure 6 shows a compilation of all 1503 SEDs ranging from the UV through the FIR binned by redshift and normalized at 1 μm. Overplotted in blue is the median SED for each redshift bin. All of the photometry used to construct these SEDs, the redshifts, and the quantities derived in this paper (such as L_{IR}) are listed in Table 3.

3.5. X-ray Properties

Using the *XMM-Newton* and *Chandra* X-ray catalogs (Brusa et al. 2009; F. Civano et al. 2010, in preparation) of the COSMOS field, we identified which of the 70 μm selected sources are detected at X-ray energies. One hundred and nineteen of the sources were detected by *XMM-Newton* and 103 by *Chandra* with 68 detected by both, for a total of 154 X-ray detected sources. The spatial distribution of the sources detected by both *XMM-Newton* and *Chandra* is shown in Figure 7. This plot illustrates the relative areas observed with both telescopes within

Table 3
COSMOS 70 μm Selected Source Catalog

| ID	Name	R.A.	Decl.	24 μm Flux[a]	70 μm Flux	160 μm Flux	Redshift	Flag[b]	$\log(L_{IR}/L_{\odot})$[c]
1017	COSMOS J100046.07+013439.89	150.19197	1.57775	0.69 ± 0.02	7.25 ± 2.13	. . .	0.518	I	11.16 ± 0.25
1077	COSMOS J100034.22+013543.18	150.14259	1.59533	1.08 ± 0.29	16.03 ± 2.03	. . .	0.23	P	10.87 ± 0.22
1081	COSMOS J100133.37+013547.59	150.38905	1.59655	0.75 ± 0.04	10.82 ± 2.00	. . .	0.23	P	10.44 ± 0.22
1082	COSMOS J100041.55+013552.68	150.17314	1.59797	1.62 ± 0.35	22.26 ± 2.45	. . .	0.37	P	11.26 ± 0.23
1083	COSMOS J100241.78+013550.07	150.15190	1.59699	0.14 ± 0.02	18.61 ± 2.12	. . .	1.20	P	12.62 ± 0.32

Notes.
[a] All fluxes and errors are in mJy. Fluxes and errors for all of the bands discussed in this paper are presented in the online version of the paper. Here, only the MIPS data points are shown as an example.
[b] Redshift Flag—D: DEIMOS spectroscopy on Keck II; Z: zCOSMOS spectroscopy from VLT/VIMOS; I: IMACS spectroscopy from Magellan; S: SDSS spectroscopy; 2dF: 2dFGRS spectroscopy; F: FORS1 spectroscopy; M: Hectospec spectroscopy from MMT; P: Photometric redshift from Ilbert et al. (2009) or Salvato et al. (2009).
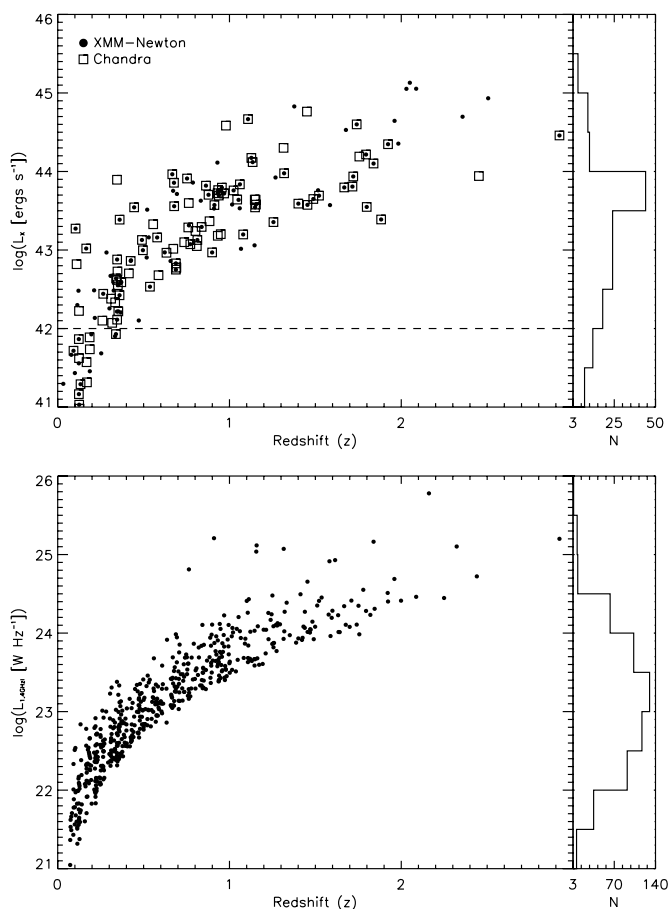[c] Total infrared luminosity and uncertainties estimated from the template fits described in Section 4.

(This table is available in its entirety in a machine-readable form in the online journal. A portion is shown here for guidance regarding its form and content.)
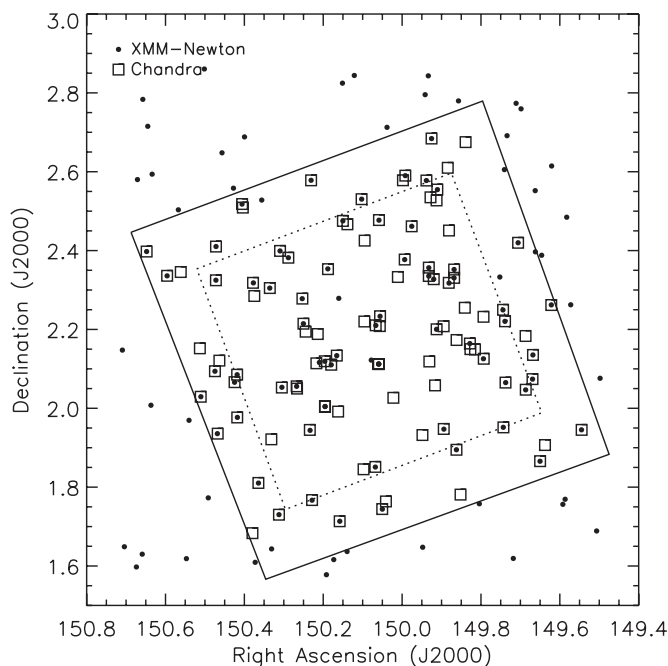
Figure 7. Spatial distribution of all the X-ray sources detected by *XMM-Newton* (dots) and *Chandra* (boxes). Note that a smaller area of the field was observed by *Chandra*. The two rectangles illustrate the different depths of *Chandra* coverage. The outer rectangle (solid box) is $\sim$0.9 deg^2 (covering 55% of the ACS area) representing the entire area observed by *Chandra*. The inner rectangle (dotted box) is $\sim$0.5 deg^2 (covering 30% of the ACS area) observed to an effective exposure time of $\sim$160 ks. The area between the two rectangles was observed to an effective exposure time of $\sim$80 ks.

Figure 8. Top: distribution of the rest-frame X-ray luminosities for the 154 sources detected by either *Chandra* or *XMM-Newton* as a function of redshift. The dashed horizontal line represents the luminosity limit above which objects are considered to be AGNs ($L_X > 10^{42}$ erg s^{-1}). Bottom: distribution of rest-frame 1.4 GHz radio luminosities for the 562 sources detected by the VLA as a function of redshift.

the ACS coverage area. The rest-frame X-ray luminosities for each of these sources was calculated from the hard band (0.5–10 keV) fluxes with an assumed power-law photon index of $\Gamma = 1.7$ and is shown in the top panel of Figure 8 as a function of redshift. One hundred and thirty two (85%) of these sources have $L_X > 10^{42}$ erg s^{-1} (dashed line in Figure 8) and so are likely to be AGNs.

Figure 9 shows the distribution of hardness ratios $((H - S)/(H + S))$, where $H = 2$–10 keV and $S = 0.5$–2 keV) for the 102 X-ray sources in the sample that are detected in both the soft and hard X-ray bands. For the remaining objects, 24 are completely hard (i.e., no detection in the soft band), 29 are completely soft (no hard band detection), and only upper limits are available for three. Overplotted on this histogram (dotted line) is the normalized distribution for the entire X-ray selected pop-

ulation that is detected in both bands. These two populations show striking differences. Whereas the full X-ray population has a hardness ratio that peaks around -0.5, the 70 μm selected population appears bimodal, with peaks at ~ -0.5 and 0.35. The 70 μm selected population of X-ray detected AGNs is on average harder than the general X-ray selected population. The large hardness ratios of some of the 70 μm sources indicate that there is significant obscuration present in these galaxies absorbing UV and soft X-ray emission.
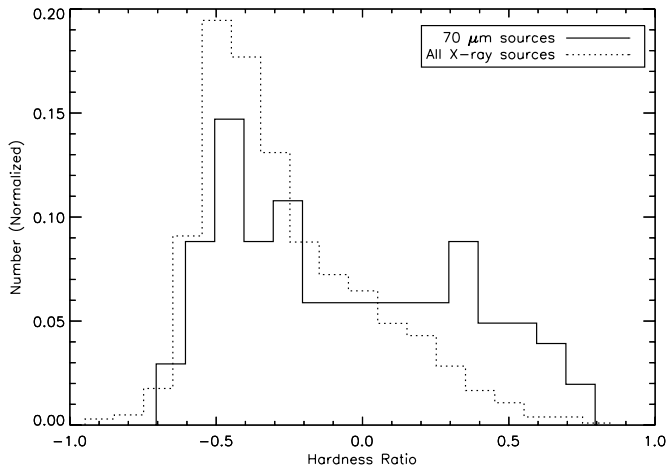
Figure 9. Normalized distribution of hardness ratios for 70 μm selected sources (solid line) and the general X-ray population (dotted line). Note that the 70 μm sample matches the general X-ray population very well at low hardness ratios but that there is an excess of 70 μm sources with larger hardness ratios.

3.6. Radio Properties

Five hundred and sixty two of the 70 μm sources were matched to a radio source within 1 arcsec. For each of these sources, we estimated the rest-frame 1.4 GHz luminosity ($L_{1.4\,\mathrm{GHz}}$) using Equation (5) of Yang et al. (2007) and applying a k-correction assuming a power law of the form $F_\nu \propto \nu^{-\alpha}$ where α, the radio spectral index, is assumed to be $\sim$0.7 (Condon 1992). The radio luminosity is presented in the bottom panel of Figure 8 as a function of redshift for all 562 radio detected sources in our sample.

Using this subsample of objects detected in both the radio and infrared, we investigated the infrared–radio correlation. Even though this correlation has been shown to hold over a wide range in redshift and luminosity (e.g., Helou et al. 1985; Condon et al. 1991a; Yun et al. 2001; Appleton et al. 2004; Ibar et al. 2008), there is some evidence that it might break down at extreme infrared luminosities or at high redshift (e.g., Kovács et al. 2006; Sajina et al. 2008; Younger et al. 2009). A complete analysis of the evolution of the infrared–radio correlation with redshift is beyond the scope of this paper; however, a full treatment of this issue will be discussed in Sargent et al. (2009). Condon et al. (1991b) found the mean value of q for BGS starbursts to be $\langle q \rangle = 2.34$ with a very small dispersion ($\sigma \sim 0.19$). This is in excellent agreement with the results from Yun et al. (2001) who found $\langle q \rangle = 2.34$ for a sample of 1809 galaxies from the *IRAS* 2 Jy sample. The Yun et al. (2001) study also found that there were slight variations in q with IR luminosity. For faint IR sources, they found values of q that were slightly higher than the mean and for bright IR sources they found a higher overall dispersion ($\sigma \sim 0.33$).

We computed the value of q as defined originally by Helou et al. (1985) as the ratio between the FIR (a combination of infrared flux measurements from 60 and 100 μm) and the flux at 1.4 GHz. We adopted this definition to allow for a direct comparison with previous work. For our sample of 562 radio detected 70 μm selected sources, we compute q using the rest-frame 60 and 100 μm flux densities obtained from the best-fit SED template and the k-corrected 1.4 GHz flux density. The resulting q distribution for our sample is shown in Figure 10 as a function of L_{IR} (top) and redshift (bottom). We find a wide range in q (0.65–3.7) with an average q of 2.36 and a dispersion
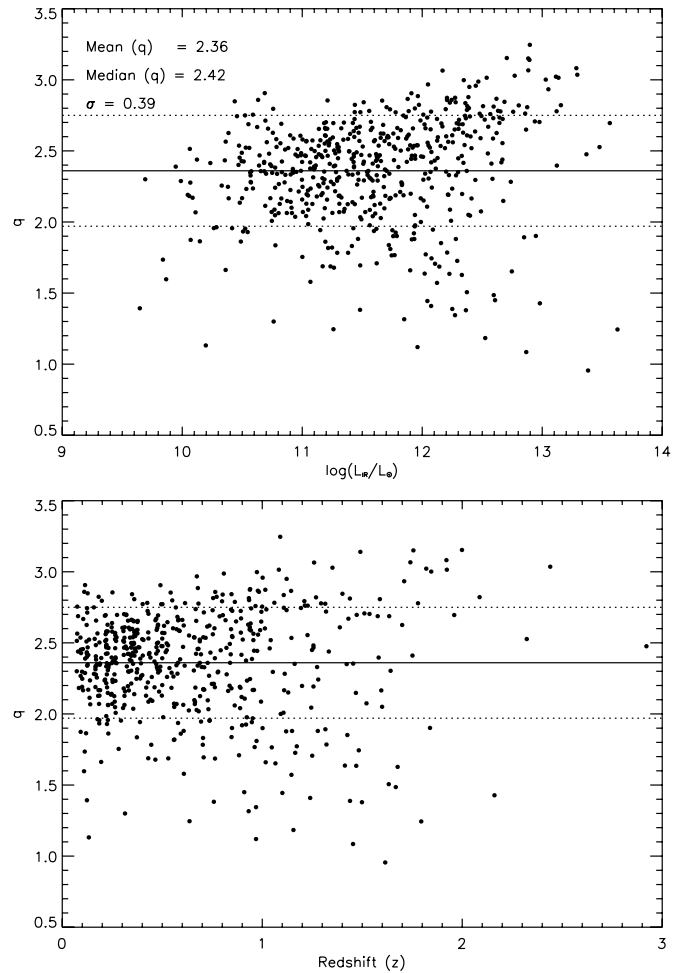
Figure 10. Radio/infrared flux ratio (q) as a function of total infrared luminosity (top) and redshift (bottom). The horizontal line represents the mean value and the dotted lines are the values $\pm 1\,\sigma$ from the mean. The scatter increases with L_{IR} and the distribution appears to bifurcate at $\sim L_{\mathrm{IR}} > 10^{12}\,L_\odot$. The large scatter at high luminosities is observed even when a more stringent (i.e., S/N > 5) cut is used.

of 0.39 overall, in agreement with previous studies. However, we find that this dispersion increases dramatically with L_{IR} with an increase in both radio-excess (small values of q) and infrared-excess (large values of q) galaxies. For the LIRGs and ULIRGs in the sample, we find $\langle q \rangle = 2.34 \pm 0.31$ and $\langle q \rangle = 2.42 \pm 0.50$, respectively. It is thought that the slightly higher mean q at high luminosities is the result of incredibly high radio free–free opacity (Condon et al. 1991b). However, we note that this effect should decrease with L_{IR} in our sample as the rest-frame radio frequency probed increases, and therefore, the infrared excess observed in these sources is not likely to be caused by this opacity effect.

4. TOTAL INFRARED LUMINOSITIES

4.1. SED Fits

We obtained the total infrared luminosity, L_{IR} (8–1000 μm), for each source in our sample by fitting the 8, 24, 70, and 160 μm data points to various SED templates using the SED fitting code *Le Phare*[22] written by S. Arnouts and O. Ilbert. We weighted each of the four points equally to avoid overweighting the points

---

[22] http://www.cfht.hawaii.edu/~arnouts/LEPHARE/cfht_lephare/lephare.html

with the smallest error bars, which are typically those at shorter wavelengths (i.e., 8 and 24 μm). The 8 μm data point was only used at low redshifts. Once it shifted below 7 μm, it was no longer used due to confusion with PAH features and since the 24, 70, and 160 μm data points well represent the portion of the SED that contributes the bulk of the infrared luminosity. Beyond $z \sim 2.4$, the 24 μm point is no longer used for the same reason.

4.2. Template Libraries

We used four different template libraries for the SED fitting— Chary & Elbaz (2001), Dale & Helou (2002), Lagache et al. (2003), and Siebenmorgen & Krügel (2007). We chose to use these template libraries since they represent a wide range of SED shapes and luminosities and they are widely used in the literature. Here, we briefly describe how each of these libraries was derived and discuss the differences between them. For more information on these template libraries, see the original papers and the detailed description in Symeonidis et al. (2008).

Chary & Elbaz (2001): this template library consists of 105 templates based on the SEDs of four "prototypical" galaxies (Arp220: ULIRG; NGC 6090: LIRG; M82: starburst; and M51: normal star-forming galaxy). They were derived using the Silva et al. (1998) models with the MIR region replaced with ISOCAM observations. These templates were then divided into two portions (4–20 μm and 20–1000 μm) and interpolated between to arrive at a set of libraries of varying shapes and luminosities. The Dale et al. (2001) templates are also included in this set to extend the range of shapes.

Dale & Helou (2002): these templates are updated versions of the Dale et al. (2001) templates which used the model of Desert et al. (1990). This model involves three components, large dust grains in thermal equilibrium, small grains semistochastically heated, and stochastically heated PAHs. They are based on *IRAS/ISO* observations of 69 normal star-forming galaxies in the wavelength range 3–100 μm. Dale & Helou (2002) improved upon these models at longer wavelengths using SCUBA observations of 114 BGS (Soifer et al. 1989) galaxies, 228 galaxies with ISOLWS (52–170 μm; Brauher 2002), and 170 μm observations for 115 galaxies from the ISOPHOT Serendipity Survey (Stickel et al. 2000). All together, these 64 templates span the IR luminosity range 10^8–$10^{12} L_\odot$.

Lagache et al. (2003): this library of starburst templates was built on the model of Maffei (1994), which uses the dust emission model of Desert et al. (1990), with a few modifications applied. First they replace the PAH portion of the templates with the one from Dale et al. (2001), then they increase the proportions of PAHs and very small grains while adding in extinction, and finally, they broaden the FIR peak and flatten the SED at long wavelengths. This library also includes templates of normal star-forming galaxies derived from the ISOPHOT serendipity survey (Stickel et al. 2000), the FIRBACK galaxy SEDs, and long-wavelength data taken from Dunne et al. (2000) and Dunne & Eales (2001).

Siebenmorgen & Krügel (2007): This template library consists of over 7000 model SEDs derived using a radiative transfer and dust model described in Kruegel (2003). This model uses the assumption of spherical symmetry and divides the starburst luminosity into two classes, that from OB stars in dense clouds (L_{OB}) and the total from all other stars ($L_{tot} - L_{OB}$). Five parameters are varied in the calculations to create the grid of template SEDs: (1) the total IR luminosity ranges from 10^{10} to $10^{14} L_\odot$, (2) the radius of the starburst nucleus: 0.35, 1, 3, 9, and 15 kpc, (3) the visual extinction of the nucleus: $A_V = 2.2, 4.5, 7, 9, 18$,

35, 70, and 120 mag, (4) the ratio of the luminosity contributed by the OB stars to the total luminosity: $L_{OB}/L_{tot} = 0.4, 0.6$, and 0.9, and (5) the dust density in the hot spots: $n^{hs} = 10^2, 10^3$, and 10^4 cm^{-3}. Combinations of parameters that are considered to be physically unlikely are left out of the final grid.

4.3. L_{IR}

For each of the above template libraries, the best-fit model was chosen by finding the one with the lowest χ^2 value and allowing for rescaling of the templates. The total infrared luminosity was then calculated from the best-fit template by integrating from 8 to 1000 μm. A sample of SEDs and the best fit from each template library is shown in Figure 11 for a range of luminosities. We visually inspected the fits and found that they typically work just as well for AGNs as for non-AGNs (in the 8–1000 μm range) since our fit does not include all of the IRAC data points which would be the most affected by an AGN. For the final L_{IR}, we adopt the value of the best fit of all the template libraries. This final value is shown in Figure 12 as a function of redshift and is presented in Table 3. Since the template library is so large, a range of templates can be used to adequately fit the data points. We use this range, along with the 1σ uncertainties in the redshift measurement, to calculate the uncertainty on the final derived L_{IR} given in Table 3. In total, we identify 687 LIRGs, 303 ULIRGs, and 31 HyLIRGs.

4.4. Effect of 160 μm Detections on L_{IR}

The depth and breadth of the 70 μm imaging in the COSMOS field allow us to obtain a more accurate measurement of the total infrared luminosity than has previously been possible for samples selected at 24 μm. The long wavelength selection means we can be confident in our estimate even at high redshifts since we are still probing the infrared slope of the SED (35 μm at $z = 1$ and 23 μm at $z = 2$). In addition, this large sample size of sources, including many that are also detected at 160 μm, enables us to statistically quantify how well we could have measured the luminosity if we only had detections in a subset of the infrared bands. This information is particularly useful for comparing our results to other studies of sources selected at 24 μm.

Figure 13 shows a comparison of our estimate of L_{IR} for the subsample of sources detected at 160 μm (463 sources in total) with the estimate excluding the 160 μm data point (based only on 8, 24, and 70 μm). The solid line represents a one-to-one relationship and the lower panel shows the difference between these two measurements. Since the majority of 70 μm selected sources are not detected at 160 μm, it is important to understand and quantify this relationship. While the internal scatter of the points is quite small ($\sigma = 0.20$ dex), there appears to be a significant offset (of 0.20 dex on average) between the estimates with and without the 160 μm data point, which increases with L_{IR}. This offset indicates that the L_{IR} determined without the 160 μm data point is underestimated by 0.20 dex on average.

In an attempt to isolate the possible cause of this offset, Figures 14 and 15 contain the same plot divided into several flux and redshift bins, respectively. The offset is largest for the sources at the faintest flux levels (0.36 dex at 4 mJy $< F(70) <$ 8 mJy) and is negligible at the brightest fluxes (0.11 dex at $F(70) > 20$ mJy). When divided into redshift bins, the largest offsets are seen at the high-redshift end. The mean offset and internal dispersion for each redshift and flux bin are summarized in Table 4. There are a few possible explanations for the observed
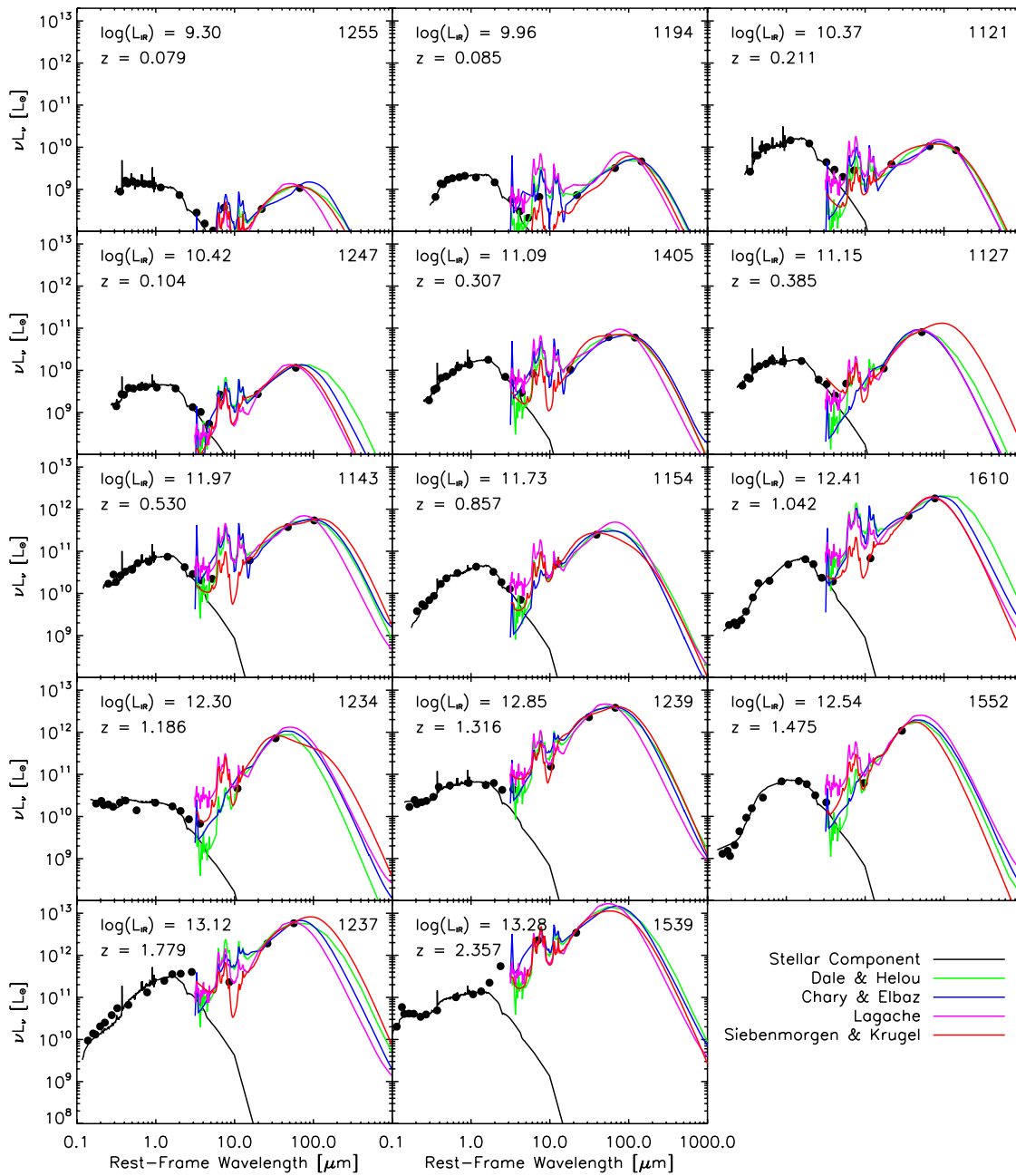
Figure 11. SEDs for a sample of 14 sources at a variety of luminosities and redshifts (both photometric and spectroscopic). Overplotted are the best-fit templates from each of the four infrared template libraries as well as the best fit to the stellar component using empirical SEDs from Coleman et al. (1980). In order to illustrate the range of fits, half of the sources here have 160 μm detections and the other half do not. Note that at high redshift both the 70 and 160 μm points are on the low-wavelength side of the peak and that the fits get progressively worse. Also, the fit to the stellar component becomes worse for sources with a significant contribution from AGN activity in the NIR (e.g., sources 1237 and 1539).

offset. One is that the intrinsic noise in the 160 μm measurement at these low flux levels biases the fit toward higher estimates than if the source was not detected at 160 μm at all. However, this explanation seems unlikely since the offset remains even when using higher S/N cuts at both 70 and 160 μm. Another possibility is that at higher redshifts the 70 μm detection samples too short a wavelength to put much of a constraint on the best-fit template. This would result in an overall larger scatter but not an offset. And finally, it is possible that the detection at 160 μm preferentially picks out sources with a colder dust component than the rest of the 70 μm population.

To test our fitting routine, we fit the same data points (8–160 μm from IRAC and MIPS) for a set of 67 local LIRGs and ULIRGs from the Great Observatory All-Sky LIRG Survey

(GOALS; Armus et al. 2009). As for the COSMOS sources, we obtained the best-fit L_{IR} with and without the 160 μm point and plot the comparison in Figure 16. For these local sources, we do not see the same offset that we see in the COSMOS sources and the intrinsic scatter is much smaller ($\sigma = 0.08$ dex). In addition, the L_{IR} obtained from this fit agrees very well with L_{IR} in the literature from the *IRAS* data points. This test gives us confidence that the offset we observe is not due to a problem with the fitting routine and also indicates that the rest-frame 70 μm data point is at a long enough wavelength to obtain an accurate measurement of L_{IR} at low redshift. We also find that the template libraries based empirically on local sources tend to fit the data points better, as is expected. As an additional test, we fit only the 8 and 24 μm data points for the local sources
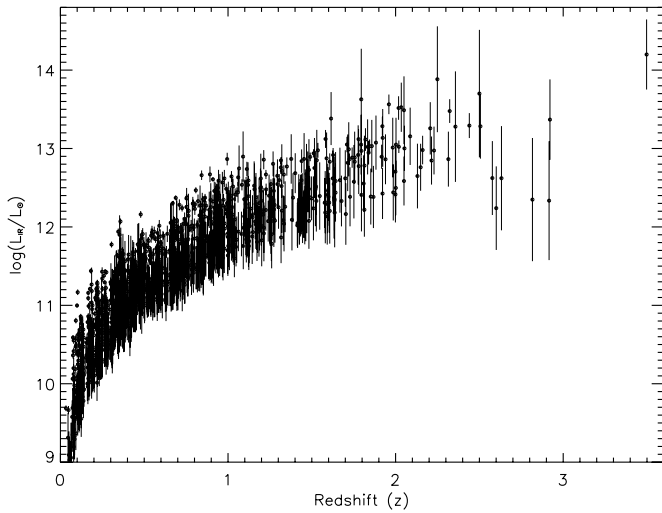
Figure 12. Total infrared luminosity (L_{IR}) as a function of redshift for all 1503 70 μm sources in the COSMOS field determined from the best-fit template using 8, 24, 70, and 160 μm where available. The error bars represent the 1σ uncertainty for each source based on the fit, the redshift errors, and a 0.2 dex systematic uncertainty for the sources without a 160 μm detection.

(roughly corresponding to observed 24 and 70 at $z \sim 2$) and find an overall scatter of ~ 0.17 dex. This result is consistent with the typical uncertainty we obtain for the COSMOS sources.

Symeonidis et al. (2008) performed a similar comparison with 43 sources from the Extended Groth Strip. They derived an empirical relation (Equation (1) in Symeonidis et al. 2008) to obtain L_{IR} directly from the 24, 70, and 160 μm flux measurements without the need to fit templates or apply k-corrections. This relation was found by summing the approximate contributions to the total infrared luminosity obtained using triangles and polygons of heights determined by the fluxes at the three MIPS wavelengths. They then add in a correction for the systematic offset found between this approximation and their total L_{IR} found through template fitting to arrive at the final equation. They found that this equation agrees well with their 43 EGS sources at all L_{IR} with a very small scatter (0.06 dex). Figure 17 shows a comparison of the L_{IR} derived here for the COSMOS sources and that using the Symeonidis et al. (2008) equation. We also find excellent agreement and a small scatter (0.06 dex overall), however, we find that the scatter increases beyond $10^{12} L_\odot$ (~ 0.1 dex). A closer inspection of the sources with the largest deviation from the equation indicates that at these redshifts, the 160 μm point is not long enough to constrain the peak of the emission and therefore, a wider range of templates fit the points than at lower redshifts.

4.5. Sources Not Detected at 160 μm

For the remaining 1042 sources without a detection at 160 μm, the relationship shown in Figures 13–15 indicates that an empirical correction may be needed. However, such a correction factor may not be warranted if those sources detected at 160 μm are intrinsically different from those not detected. Figure 18 shows the distribution of 70 μm fluxes for these two subsamples. The sources detected at 160 μm are clearly weighted toward the bright end of the flux distribution.

To further examine the properties of the sources not detected at 160 μm, we fit templates to their mean SED using a stacked 160 μm data point in several redshift and flux bins in the same manner as the detected sources. The resulting comparison is shown as the colored points in Figure 19. While these stacked
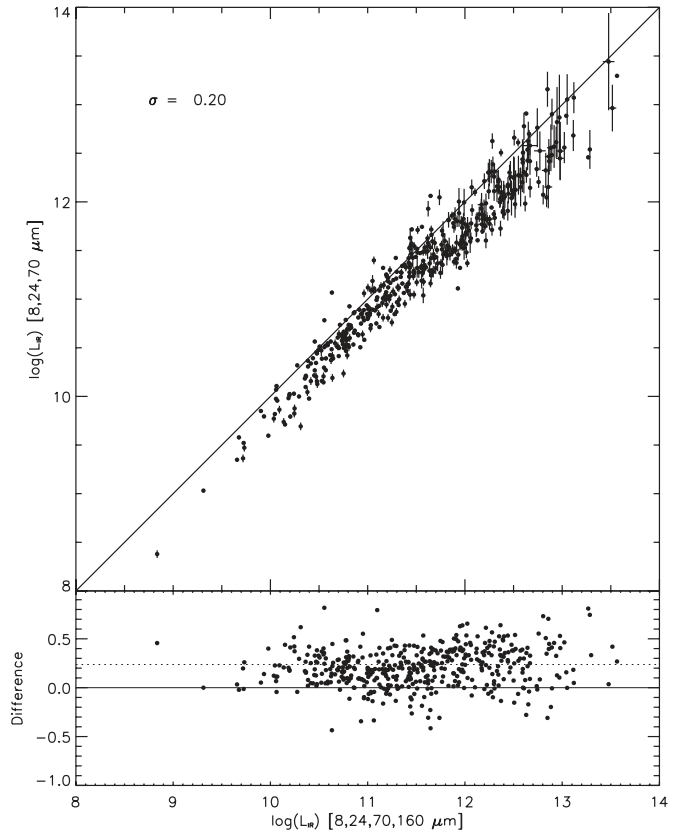

Figure 13. Comparison of the total infrared luminosity for the 463 sources detected at 160 μm obtained with and without the 160 μm data point. The error bars are the 1σ uncertainty based on the template fit. The bottom panel shows the difference in L_{IR} between these two measurements. The mean offset is shown as the dotted line and the dispersion about this mean is given.

points show a similar amount of scatter as the 160 μm detected sources, they do not show the same systematic offset. For the stacked sources, the luminosity obtained with the 160 μm point is in agreement with the luminosity obtained without it. This suggests that the sources detected at 160 μm are indeed biased toward colder sources. Therefore, a correction to the L_{IR} for the rest of the 70 μm sample is not necessary. Instead, we include the scatter in the relationship as an additional source of uncertainty and include this in our error bars in Figure 12. Thus, the typical uncertainty for sources detected at 160 μm is 0.05 dex, while for those not detected it is ~ 0.2 dex.

4.6. Estimates Based on 24 μm

Since MIPS is the most sensitive at 24 μm, samples selected at this wavelength are very useful and will continue to be used in the future. Therefore, it is essential to understand how well their total infrared luminosities can be determined with just this data point. To test this, we obtained the best-fit template using just the 24 μm data point. Since there is only one point, the templates are not really fit but instead the best match to the 24 μm flux at the source redshift is obtained from each of the template libraries without allowing for rescaling. For the final luminosity estimate, we chose to use the Siebenmorgen & Krügel library since it was the best match for the vast majority of sources using 70 and 160 μm and has the largest variety of SED shapes. Figure 20 shows the comparison between luminosity estimates using all available bands and using only the 24 μm point for both 160 μm detected and non-detected sources. The scatter in this relationship is much larger ($\sigma \sim 0.4$ dex) and
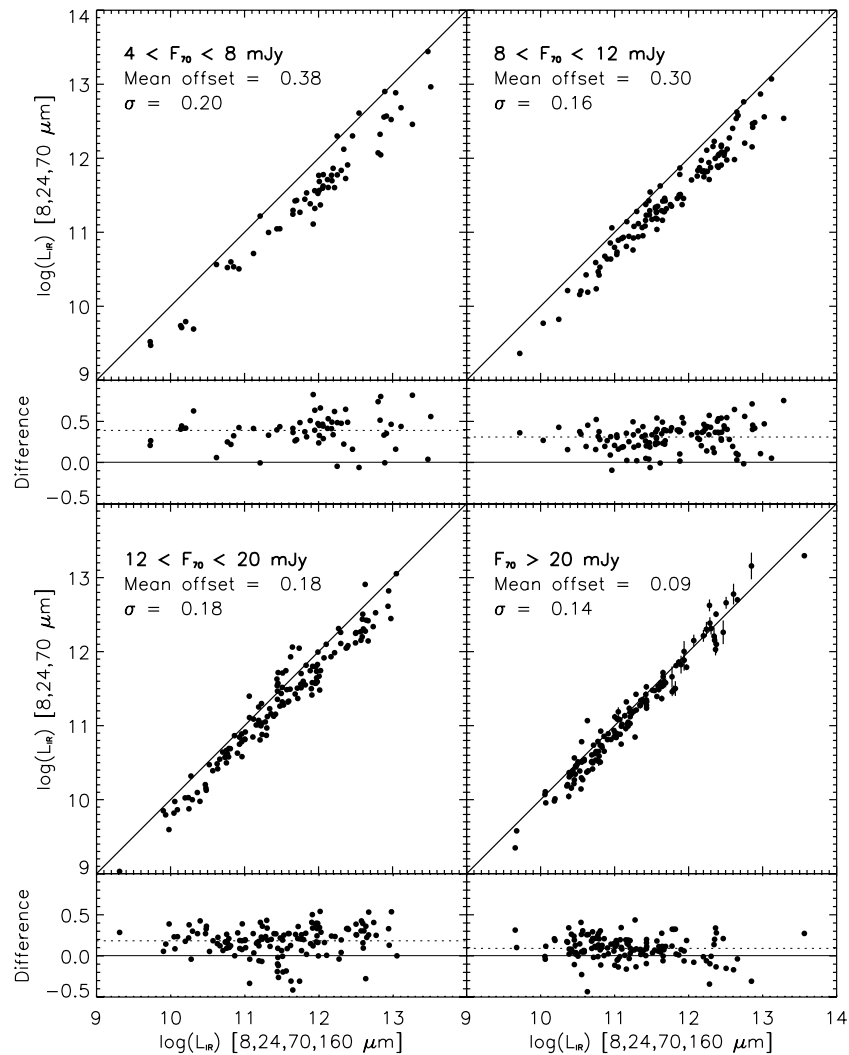
Figure 14. Same as Figure 13 but divided into four 70 μm flux bins. Note that the mean offset between the two luminosity estimates decreases at higher 70 μm fluxes, while the overall scatter stays about the same.

the difference can be up to 1 dex for some sources. A larger offset is also seen for the sources detected at 160 μm than those not, consistent with the results discussed in the previous section. The large scatter indicates that luminosity estimates for samples based solely on 24 μm detection alone can be off by a significant amount and many LIRG and ULIRG samples in the literature based on 24 μm may actually be contaminated by lower luminosity sources since their number densities are higher though it is possible that this effect is mitigated by the slight offset (~ 0.1 dex on average) obtained without the 70 μm data point.

5. DISCUSSION

In this paper, we have presented a sample of 1503 70 μm sources in the COSMOS field and determined a reliable measure of their total infrared luminosity. We believe that this is the largest sample of 70 μm sources to date. When the source is detected at 160 μm, we obtain an estimate of L_{IR} accurate to within 0.05 dex on average and 0.2 dex for those without a 160 μm detection. This result is much better than can be obtained from a 24 μm data point alone (~ 0.5 dex). In this section, we discuss in more detail the UV-to-FIR SEDs and the variations of the mean SED shape with L_{IR}. In particular, we explore three spectral regions (the UV, NIR, and MIR) since these have been

found to be the most sensitive to the underlying power source (i.e., starbursts and AGNs). We make use of the multiwavelength properties of the sample to identify a large population of AGN candidates.

5.1. Analysis of SEDs

Figures 6 and 21 show the full range of SEDs that we observe for the 70 μm selected sample of galaxies binned by redshift and L_{IR} with the median SED in each bin overplotted as a blue line. The median SEDs are similar to sources observed locally for sources at low luminosity (e.g., Dale et al. 2007; SINGS, $L_{IR} < 10^{11} L_\odot$) and at high luminosity (e.g., V. U et al. 2010, in preparation; RBGS, $L_{IR} > 10^{11} L_\odot$). All of these studies have shown that the median UV-to-FIR SEDs have two prominent thermal peaks (the optical stellar peak and the FIR dust peak) and, in addition, a range of spectral shapes, particularly in the UV (0.2–0.5 μm), NIR (2–5 μm), and MIR (10–30 μm). With the large number of sources in our 70 μm sample, we can finally begin to quantify the full extent of these variations and explore how different parts of the SED correlate with each other and with L_{IR}. As should already be known from studies of smaller samples of local objects (e.g., RBGS: Sanders et al. 2003; 1 Jy ULIRG Survey: Kim & Sanders 1998), it is clear that a single archetypical template for a given infrared luminosity (e.g.,
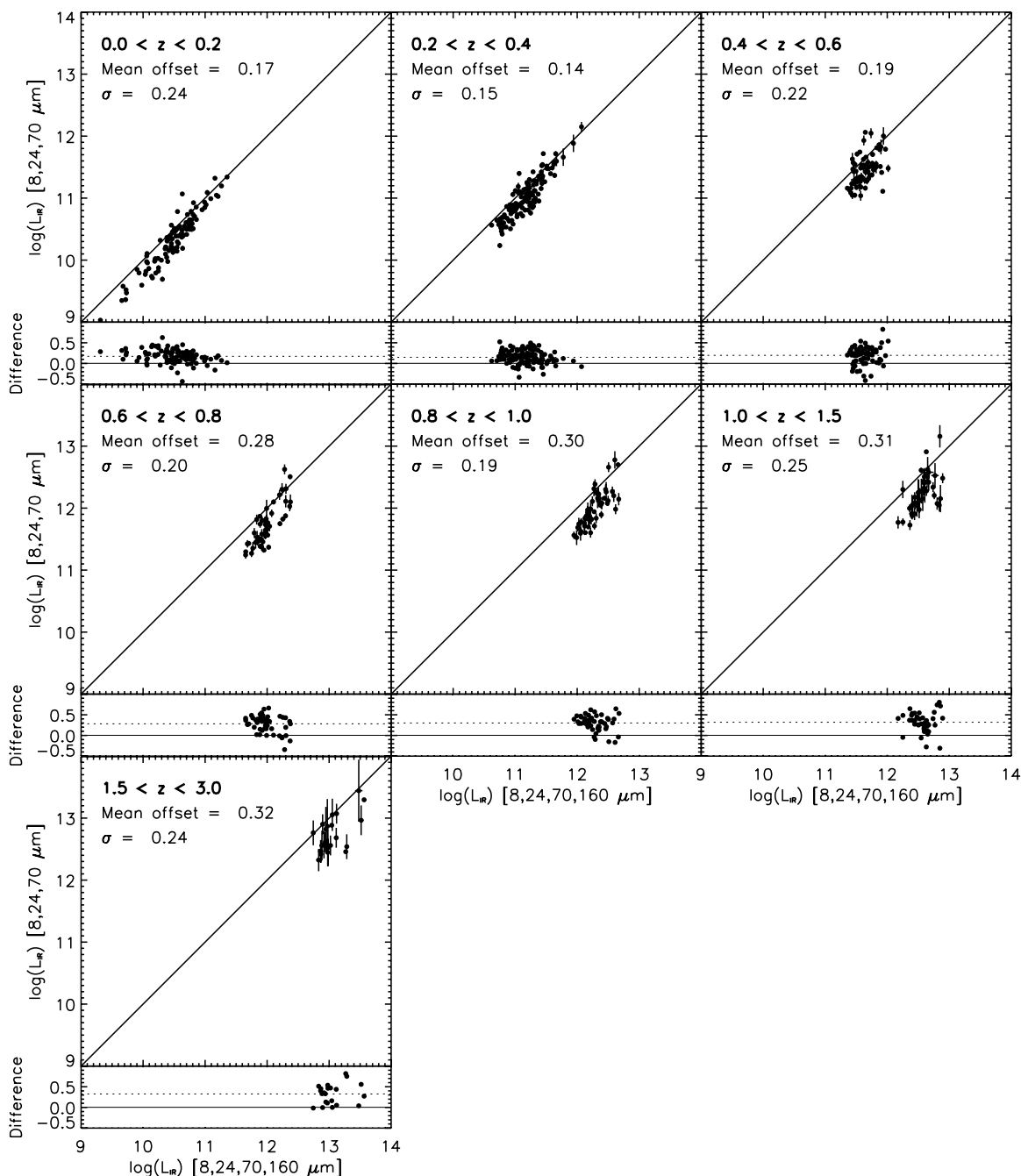
Figure 15. Same as Figure 13 but divided into seven redshift bins. Note that the mean offset between the two luminosity estimate increases with redshift, while the overall scatter stays about the same.

Table 4
Offset in L_{IR} Estimate Without 160 μm Data Point

| Flux Bin (mJy)	z Bin	Med (Flux) (mJy)	Med (z)	No. of Sources	Mean Offset	Dispersion
0.4–0.8	...	6.6	0.84	61	0.41	0.20
0.8–12.0	...	9.4	0.58	117	0.33	0.16
12.0–20.0	...	14.7	0.41	140	0.20	0.18
> 20.0	...	32.8	0.22	141	0.09	0.14
...	0.0–0.2	24.8	0.12	106	0.17	0.16
...	0.2–0.4	15.9	0.27	124	0.14	0.15
...	0.4–0.6	12.8	0.49	69	0.19	0.22
...	0.6–0.8	12.2	0.69	49	0.28	0.20
...	0.8–1.0	11.4	0.90	50	0.30	0.19
...	1.0–1.5	10.6	1.15	39	0.31	0.25
...	1.5–3.0	8.3	1.78	22	0.32	0.24
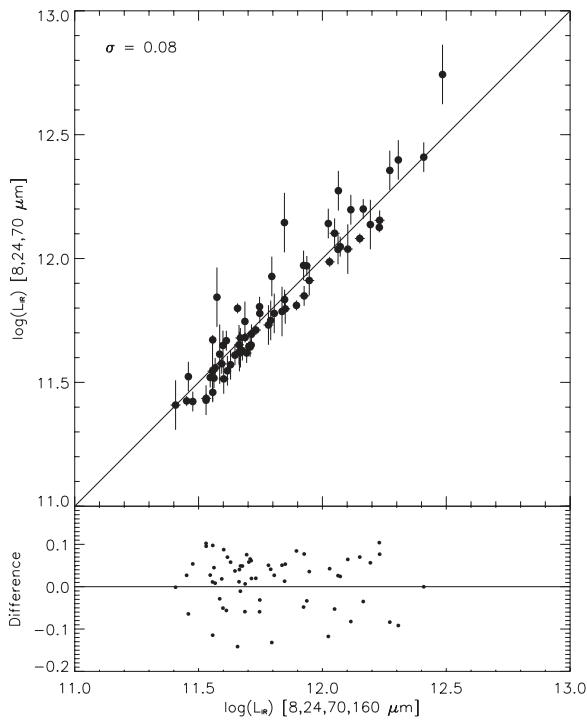
Figure 16. Comparison of the total infrared luminosity obtained with and without the 160 μm data point for a sample of 67 local (U)LIRGs from the GOALS survey. The low dispersion obtained between these two measures indicates that the template fitting method is reliable and that the rest-frame 70 μm data point is long enough to obtain a reliable measure of $L_{\rm IR}$ at low redshift ($z < 0.1$).

Arp 220 or Mrk 231 for ULIRGs) would not be applicable for all objects with that luminosity.

The median SEDs clearly show several general features. First, most of them show the 1.6 μm peak of the stellar bump. This feature becomes less pronounced at higher luminosities. The SEDs also display a prominent 5 μm dip at low luminosities which becomes less clear at high luminosities. The 7.7 μm PAH emission feature is also evident at $L_{\rm IR} < 10^{11} L_\odot$ near 8 μm but becomes less evident in the higher luminosity bins as rest frame 7.7 μm is no longer probed. However, in the highest luminosity bins, 24 μm approaches rest-frame 7.7 μm and this enhancement is still not observed, possibly due to the median SED being dominated by AGNs at those luminosities. Many of the SEDs show an increase in emission toward the UV, indicative of the big blue bump (Malkan & Sargent 1982; Sanders et al. 1989; Elvis et al. 1994) seen in many AGNs. The *GALEX* data points, particularly at high redshift where they probe further into the FUV, point to a broad maximum for many of these sources.

To provide a more quantitative measure of the spread in SED shapes, we compute three spectral indices (logarithmic rest-frame νL_ν ratios) probing three different wavelength regimes: UV/optical from 0.2 to 0.5 μm ($\alpha_{0.2}^{0.5}$), NIR from 2 to 5 μm (α_2^5), and MIR from 10 to 30 μm (α_{10}^{30}). These spectral indices are plotted against each other in Figures 22–24 binned by $L_{\rm IR}$. All three of these plots show strong trends with $L_{\rm IR}$. α_2^5 increasing with $L_{\rm IR}$ as sources become dominated by power-law SEDs (see Section 5.2). This is also evident in Figure 24 where the sources with high α_2^5 form a separate distinct branch at intermediate values of α_{10}^{30}. For galaxies with low values of α_2^5, α_{10}^{30} is low at low luminosities and steadily increases with $L_{\rm IR}$. $\alpha_{0.2}^{0.5}$ spans a wide range at all $L_{\rm IR}$ (a range of nearly 3 orders of
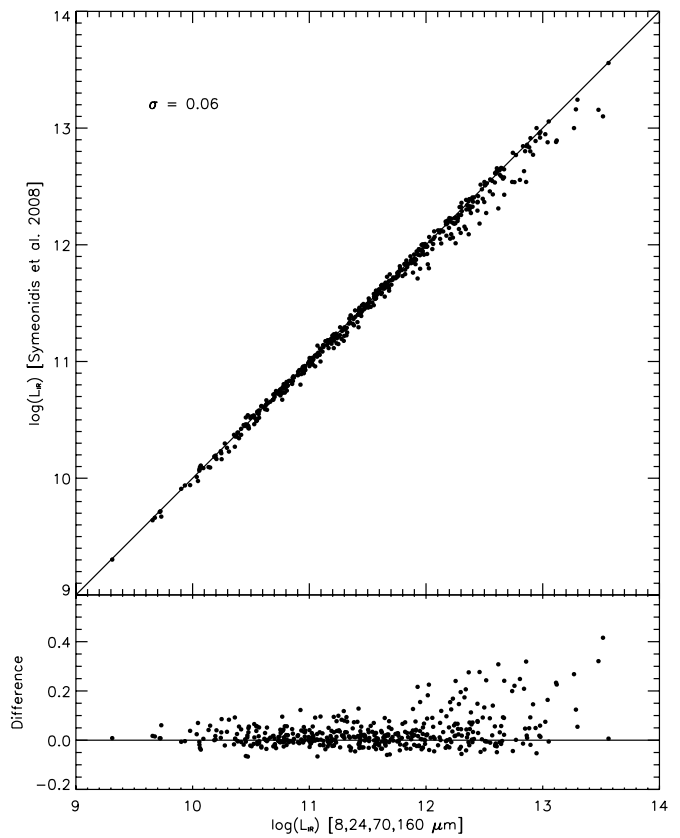
Figure 17. Comparison of the total infrared luminosity obtained with the fits to the four infrared data points to that obtained with Equation (1) of Symeonidis et al. (2008). The agreement between our estimates and the equation is excellent although the dispersion increases at $L_{\rm IR} > 10^{12} L_\odot$. At these higher luminosities, and consequently higher redshifts, the 160 μm data point is not long enough to precisely constrain the peak and thus there is a larger spread among the best-fit templates.
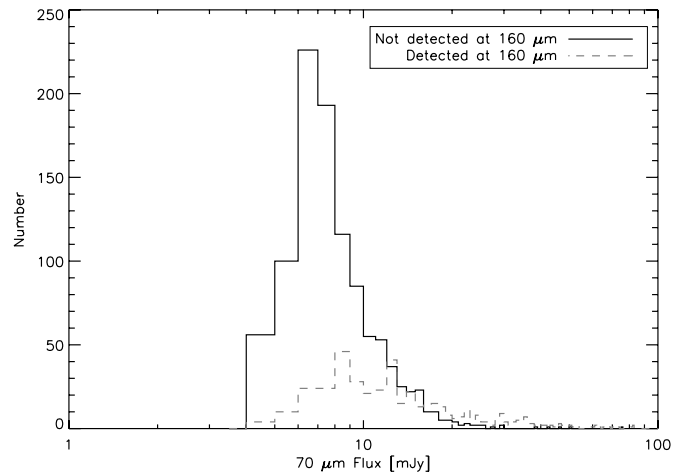
**Figure 18.** 70 μm flux distribution of the 463 sources detected at 160 μm (gray dashed) and the 1042 not detected at 160 μm (solid black). On average, those detected at 160 μm have higher 70 μm fluxes.

magnitude) and has lower values on average at the most extreme luminosities.

5.1.1. 160/70 μm Flux Ratios

In addition to the SED shapes described above, our large 70 μm sample and the substantial number of detections at 160 μm makes it particularly useful to investigate the
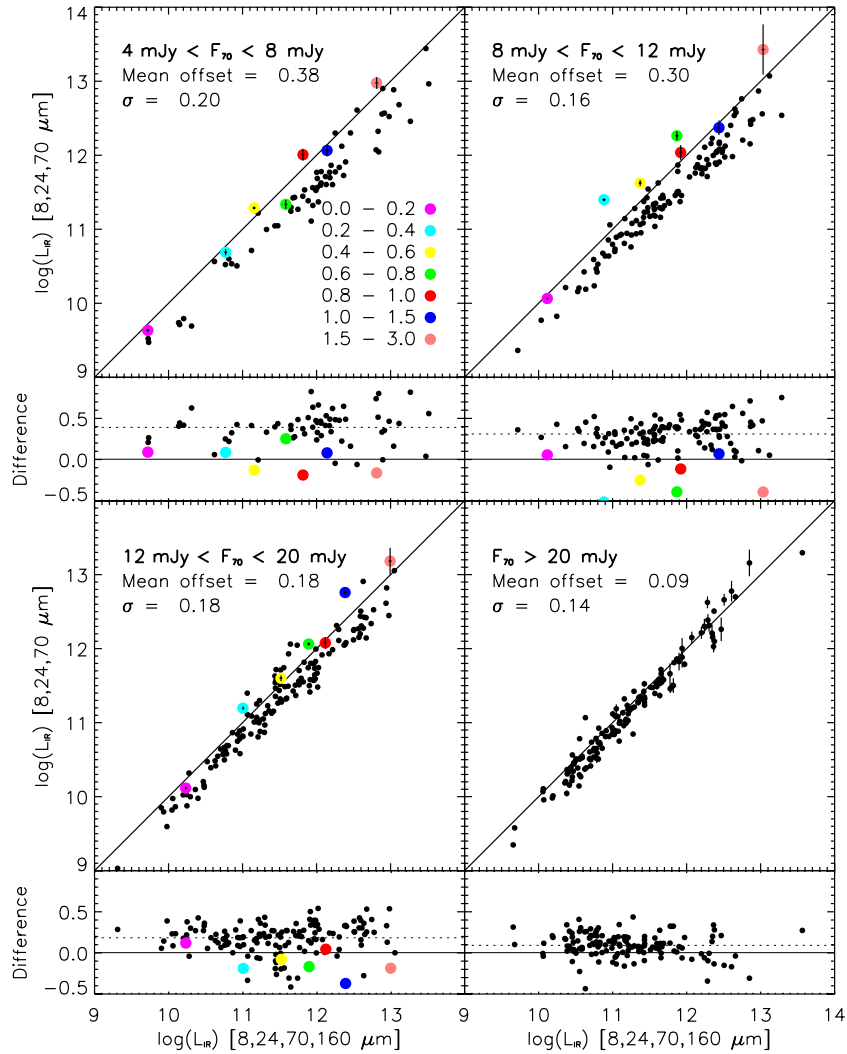
Figure 19. Same as Figure 14 but with the luminosities obtained by fitting the mean SED for the 1042 sources not detected at 160 μm with stacked 160 μm flux measurements divided into several flux and redshift bins (shown as colored points). Note that while the stacked points show the same amount of scatter overall between the two luminosity estimates, they do not have the same systematic offset as the 160 μm detected sources. This suggests that there is an intrinsic difference in the shape of the SEDs between sources with a 160 μm detection and those without.

160/70 μm flux ratios as a crude measure of the characteristic dust temperature for the FIR peak emission. Figure 25 shows the observed FIR colors ($\nu F_\nu(160)/\nu F_\nu(70)$) as a function of redshift and L_{IR} for all 70 μm sources detected at 160 μm. For those not detected at 160 μm, the colored points on the plot represent the colors obtained from their stacked 160 μm fluxes. To put these values in context we also overplot the flux ratios for local *IRAS* 60 μm selected sources from the RBGS over a wide range of L_{IR} (10^8–$10^{12.5}$ $L_\odot$) with MIPS observations obtained as a part of GOALS or the Spitzer Infrared Nearby Galaxies Survey (SINGS; Kennicutt et al. 2003; Dale et al. 2007). A typical error bar for the sources detected at 160 μm is shown in the corner. The overall scatter of the data points remains the same even with a cut at larger S/N, indicating that the observed trends are likely real. The local sources span a large range in $\nu F_\nu(160)/\nu F_\nu(70)$ from 0.2 to 5 and show a strong trend with L_{IR}. Also overplotted in gray are a set of values obtained from the Dale & Helou (2002) templates spanning an L_{IR} range of $10^{8.3}$–$10^{13.5}$ from top to bottom as a function of redshift. These templates span most of the range occupied by the COSMOS 70 μm selected sources (the full set of libraries covers the entire range of colors observed at each redshift but we show just this one library for illustration). The sources not detected at 160 μm

span the lower portion of the range occupied by the sources detected at 160 μm. This result is expected if the 160 μm detection preferentially selects colder sources than the rest of the sample.

We obtained rest-frame $\nu F_\nu(160)/\nu F_\nu(70)$ values by using the 70 and 160 μm fluxes determined from the best-fit IR template used to estimate L_{IR}. These values are plotted in Figure 26 as a function of redshift and luminosity. As a note of caution, since these values are dependent on the best-fit SED template this adds an extra source of uncertainty, particularly at the high-redshift end (where shorter rest-frame wavelengths are observed). We find that the COSMOS sources span the same range of colors (and thus dust temperatures) as the local sources but that there is an apparent excess of colder sources at higher luminosities, similar to the result of Symeonidis et al. (2009). However, our interpretation is that this excess is likely a result of the longer wavelength selection (rest-frame 80 μm at $z \sim 1$ versus 60 μm locally) and the fact that the peak of emission is not well constrained at these redshifts and thus a wide range of templates can fit the data points. Future surveys at FIR and submillimeter wavelengths with *Herschel* and SCUBA2 will be able to disentangle the temperature-dependent selection effects and investigate the dust temperature distributions of high-redshift galaxies.
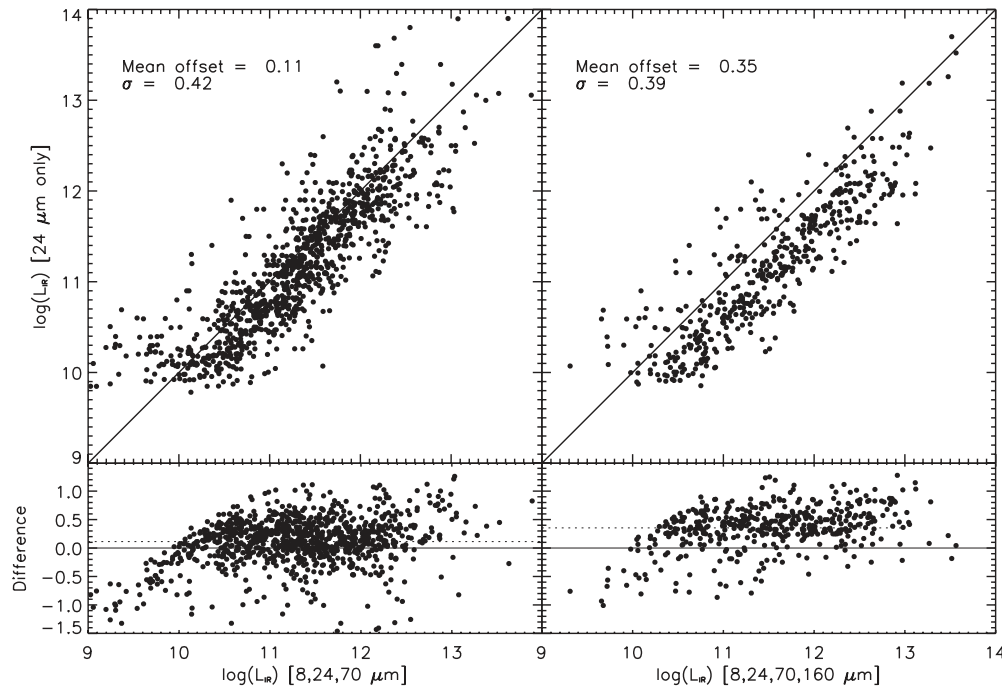
Figure 20. Comparison of luminosities obtained with all the available bands for the sources without 160 μm detections (left) and those with 160 μm detections (right) to the luminosities obtained from just the 24 μm data point. The dotted line represents the mean difference between the two and the σ value is the internal dispersion about that mean. The sources detected at 160 μm show a similar offset in their luminosities as they did in the 70/160 μm luminosity comparison (see Figure 13). This is a further indication that the sources detected at 160 μm are intrinsically different (i.e., have a colder dust component) than those that are not.

5.2. AGN Diagnostics

Both X-ray and radio detections are traditional methods used to identify potential AGNs in high-redshift galaxies. The vast majority of the 70 μm selected galaxies that are detected in the X-ray (86%) have an X-ray luminosity greater than 10^{42} erg s^{-1} and are therefore bona fide AGNs. The 22 lower luminosity sources are all at low redshifts ($z < 0.35$). Most of the X-ray detected AGNs have power-law SEDs (though not all), particularly at high L_{IR}. Many sources that are not detected as AGNs in the X-ray also have a power-law SED. These are possibly heavily obscured (Compton thick) AGNs that are opaque even to hard X-ray emission (Polletta et al. 2006).

Since α_2^5 is a measure of the νF_ν slope between 2 and 5 μm, it is therefore a good way to select power-law galaxies. Anything above zero on the y-axis of Figure 22 or the x-axis of Figure 24 has the shape of a power law in the NIR, i.e., these objects neither have a strong 1.6 μm bump nor a dip at 5 μm. The $\alpha_2^5 > 0$ cutoff here corresponds to a F_ν spectral slope of 0.4 (similar to what is used as a power-law slope cutoff in the literature, e.g., Alonso-Herrero et al. 2006 and Donley et al. 2007). X-ray detected AGNs span almost the entire area of the spectral index plots rather than being clearly separated the way the power-law galaxies are. However, they do on average have lower α_{10}^{30} as AGNs in the local universe do.

We select all sources with $\alpha_2^5 > 0$ to be power-law AGN candidates. A total of 166 (11.2%) objects satisfy this criterion. Forty five of these are detected in the X-ray ($\sim 27\%$; a slightly lower fraction than found by Alonso-Herrero et al. 2006 and Donley et al. 2007 but consistent with the shallower COSMOS X-ray depths). A few differences between power-law galaxies detected in the X-ray and those not detected in the X-ray can be seen in their SEDs. Those sources detected in the X-ray tend to display the full range of properties in the UV where only one or two sources that are not X-ray detected appear bright in the

UV. The prominence of the UV emission in the X-ray detected power-law galaxies could be evidence that these sources tend to be less obscured than the non-X-ray-detected sources and hence are transparent to UV (and X-ray) emission. The SEDs of the non-X-ray detected power-law galaxies also tend to have a steeper slope.

We use the infrared–radio correlation as another way to investigate the energy source. Using the limits defined in Yun et al. 2001; five times larger radio or IR flux than expected from the infrared–radio correlation) for radio-excess ($q < 1.64$) and infrared-excess ($q > 3.0$) objects we find many objects that fall into these two categories. In total there are 27 radio-excess sources, six of which (22%) are also detected as X-ray AGNs (as shown in Figure 27). The fraction of objects that this population represents increases with L_{IR} from 4 (2%) at $< 10^{11} L_\odot$, to 5 (2%) LIRGs and 16 (14%) ULIRGs. Radio-excess sources are believed to be potential AGN hosts where the extra radio emission seen comes from either a compact radio core or from associated radio jets or lobes (Sanders & Mirabel 1996).

All 14 of the infrared-excess objects are ULIRGs or HyLIRGs and represent 11% of the sample at these luminosities. Six (43%) of them are X-ray detected AGNs. A total of 25 of the obscured AGN candidates (64%) described in Section 5.2.2 are detected in the radio and have $\langle q \rangle = 2.54 \pm 0.63$. Five of these (two X-ray AGNs) are infrared-excess objects. It is interesting to note that the IR excess objects contain a higher fraction of X-ray detected AGNs than the radio-excess objects. It is also interesting to note that many of the radio- and infrared-excess sources also have a power-law SED (see Figure 27).

5.2.1. IRAC Color Selected AGNs

Color selection in the MIR has also been shown to be an effective way to select potential AGNs (Stern et al. 2005; Lacy et al. 2004) as these colors can separate star-forming galaxies
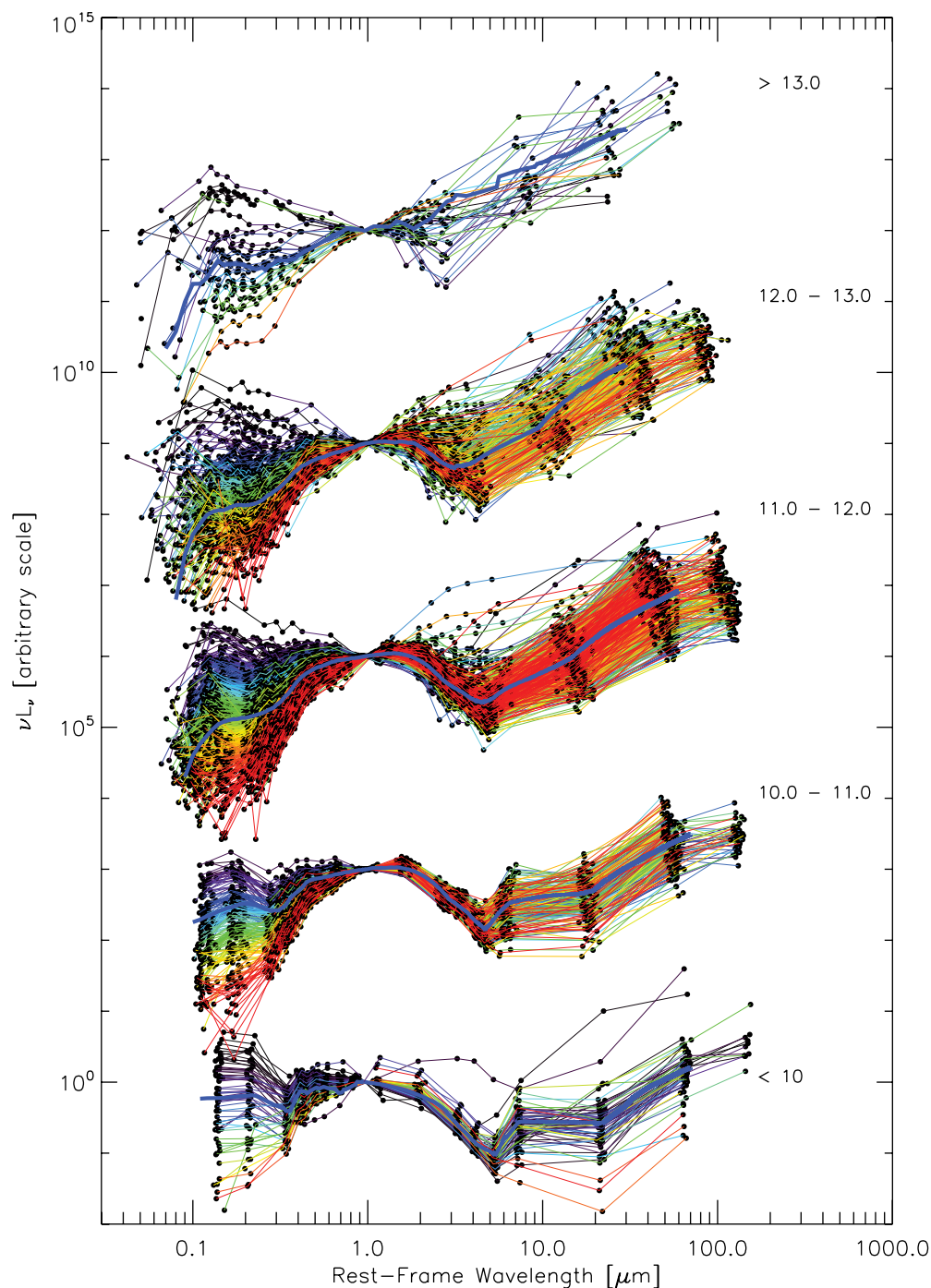
Figure 21. SEDs of all 1503 70 μm sources binned by luminosity and normalized at 1 μm. The SEDs are color coded such that the ones with the bluest slope in the UV–optical are purple/blue and the reddest are red and the spectrum in between shows the range of SED colors. The median SED for each bin is overplotted in blue. Note the large variety in SED shapes, particularly in the UV, and the trends with L_{IR}. At the highest luminosities, there is an obvious trend toward power-law SEDs all the way from the optical through the FIR.

(A color version of this figure is available in the online journal.)

with a stellar bump at 1.6 μm from those with a power-law-like SED. Also, this method can potentially find dust-obscured AGNs since the MIR wavelengths are not as affected by extinction as the UV and optical. Following the criteria of Stern et al. (2005), we used the color–color IRAC plot (see Figure 28) to select potential AGNs and compare these sources with those found using four other methods. A total of 232 sources meet the Stern et al. criteria, representing $\sim$ 15% of the entire 70 μm sample. Of these 232, 82 (35%) are detected as AGNs in the X-ray. This is 62% of the total X-ray AGN population, which

means the other 50 X-ray AGNs are not selected by this method. According to Stern et al., this method is good at selecting broad-line AGNs (selects $\sim$ 91%) and not as good at selecting narrow-line AGNs ($\sim$ 40%) with an overall contamination rate of $\sim$ 20%. Donley et al. (2007) show that this region of the plot can be contaminated by starburst-dominated ULIRGs (like Arp 220) and normal star-forming galaxies. If we assume that 20% of the 232 objects are potentially contaminants, this leaves us with 186 actual AGNs, or about 1.5 times the number detected in the X-ray. Of the potentially obscured objects described in
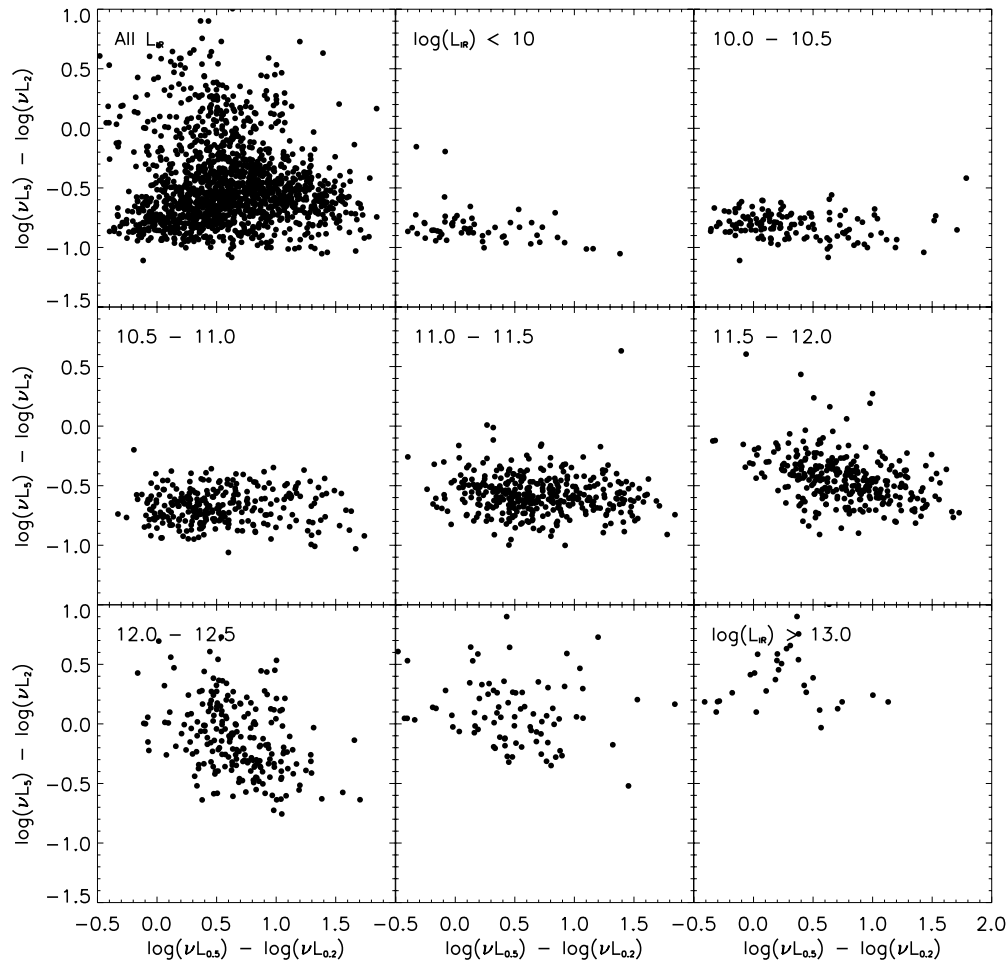
Figure 22. Rest-frame NIR spectral index (α_2^5) vs. UV/optical spectral index ($\alpha_{0.2}^{0.5}$) divided into L_{IR} bins. Note the large range spanned by both indices. α_2^5 increases with L_{IR} as more sources become dominated by a power-law SED, while $\alpha_{0.2}^{0.5}$ spans a large range at all luminosities.

the following section ($F(24\,\mu m)/F(R) > 10^3$), 36 out of the 60 match these color criteria as do 33 out of the 56 that also have $R - K > 4.5$. Most of the power-law galaxies (62%) fall in a narrow region in the Stern et al. (2005) selection box but many ($\sim 35\%$) fall outside this region. Very few of these objects fall in the lower left corner of the selection region, indicating that this is possibly the region that contributes most of the contamination in the selection (consistent with the results of Donley et al. 2008). Thirteen of the radio-excess sources are also selected by the Stern et al. criteria.

5.2.2. Obscured AGN Candidates

Fiore et al. (2008, 2009) have shown that obscured AGNs tend to have high MIR-to-optical flux ratios and red $R - K$ colors. The 24 μm to R-band flux ratio for each of the 70 μm sources in the sample is shown in Figure 29 as a function of $R - K$ color with AGNs selected through four other methods overplotted. The dotted lines show the cuts of $(R - K)_{\rm Vega} > 4.5$ and $F(24\,\mu m)/F(R) > 10^3$ defined in Fiore et al. (2008) for selecting candidate-obscured AGNs at high redshift. Fifty six of the galaxies in our sample make both of these cuts and 14 of them are detected in the X-rays. Three are detected only in the hard band and one only in the soft band. The remaining sources have a median hardness ratio of 0.2. The redshifts of these galaxies range from 0.7 to 2.5 with the median being $z = 1.5$, confirming the results of Fiore et al. (2008). Additionally, four

galaxies match the MIR-to-optical flux ratio criteria but are bluer than the $(R - K)_{\rm Vega} > 4.5$ magnitude cutoff. Of these, one is detected as an AGN in the X-ray with a detection only in the hard band. These four sources have redshifts that range from $z = 1.2$ to 2.4 with a median redshift of 2.1—a similar distribution to the sources with red $R - K$ colors. The 24 μm to R-band flux ratio correlates with the total infrared luminosity (as expected for obscured AGNs where the luminosity from the nuclear regions is greatly reduced by the obscuring material) and those above the cutoff of 10^3 are predominantly ULIRGs and HyLIRGs. We consider all 61 of these galaxies to be obscured AGN candidates.

It is also worth noting that this selection is similar to other IR/optical color selections in the literature, such as dust-obscured galaxies (Dey et al. 2008) and infrared bright, optically faint galaxies (Yan et al. 2004; Houck et al. 2005; Weedman et al. 2006). The dust-obscured galaxy color cut ($R - [24] > 14$) is actually the same as the one used here and is expected to select high-redshift ($z \sim 2$) extremely luminous galaxies with large column densities of dust.

5.2.3. AGN Fraction Among Luminous and Ultraluminous Infrared Galaxies

In the local universe, the AGN fraction of galaxies is known to increase very strongly with L_{IR}. Using spectroscopic diagnostics of a sample of 200 luminous infrared galaxies from *IRAS*, Veilleux et al. (1995) found that 62% of objects at the highest
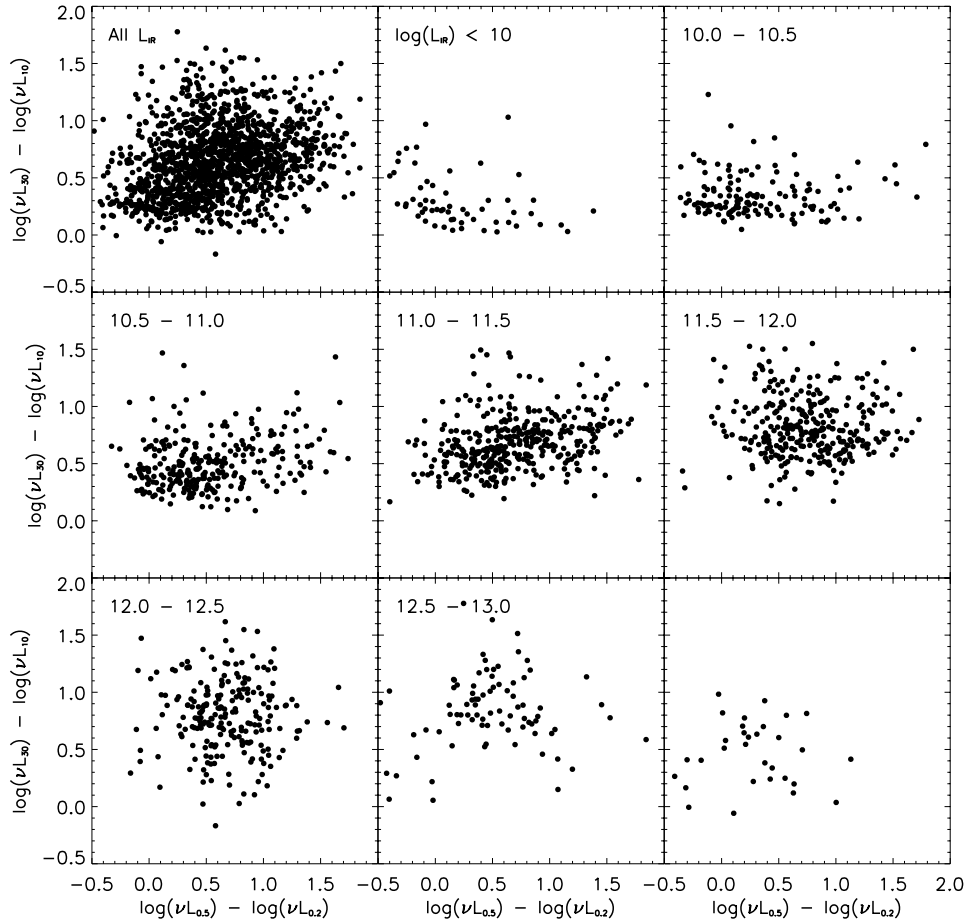
Figure 23. Rest-frame MIR spectral index (α_{10}^{30}) vs. UV/optical spectral index ($\alpha_{0.2}^{0.5}$) divided into L_{IR} bins. Note that α_{10}^{30} appears to span a larger range in values with increasing L_{IR}.

luminosities were AGNs. A similar study of the 1 Jy sample of ULIRGs (Veilleux et al. 1999) found that above $L_{IR} > 10^{12.3}$, $\sim$50% of objects are AGNs. Tran et al. (2001) found a similar transition luminosity of $L_{IR} > 10^{12.4} L_{\odot}$ between objects whose luminosities are dominated by starburst emission and those dominated by AGNs. Above this transition they found that "most ULIRGs appear AGN-like." With the large sample of objects over the wide range of luminosities probed by our 70 μm selected sample, we can address the question of whether this trend holds out to higher redshifts.

Table 5 shows the total number of galaxies in each L_{IR} bin along with the number of X-ray detected sources over the full area, in the area covered by *Chandra*, and in the area with the deepest *Chandra* coverage. The total fraction of X-ray detected AGNs increases with increasing L_{IR}, from 5% at $L_{IR} < 10^{10} L_{\odot}$ to $\sim$15% for ULIRGs and $\sim$42% for HyLIRGs, however, these numbers are lower limits due to the uneven X-ray coverage across the field. The fraction increases when limited to the smaller areas with deeper X-ray coverage, though the small numbers make a statistical analysis difficult. This indicates that as many as 12% of LIRGs, 30% of ULIRGs, and 43% of HyLIRGs are AGNs with detectable X-ray emission. For the rest of the discussion here, we use the fractions obtained over the entire area.

Table 6 shows the fraction of candidate AGNs found by each method (including X-ray detected, radio selected, IRAC color selected, power-law galaxies, and potentially obscured objects). If we add up all of the galaxies that fall into any of the possible AGN candidate categories (total column in Table 6), then we

find that the AGN fraction ranges from 3% at $L_{IR} < 10^{10} L_{\odot}$ to $\sim$70%–100% for ULIRGs and HyLIRGs (illustrated in Figure 30). There is likely to be some contamination in this estimate, particularly from the IRAC color selection method. If we leave out the IRAC selected objects, the AGN fraction goes from 2% for objects with $L_{IR} < 10^{10} L_{\odot}$ to 10% for LIRGs, 51% for ULIRGs, and 97% for HyLIRGs. This result is in excellent agreement with the AGN fraction in the local universe, indicating that high-redshift ULIRGs are indeed similar to local sources in this respect.

The redshift and L_{IR} distribution for the AGN candidates found using each method is shown in Figure 31. Those objects that are also selected in the X-ray are shown by the filled histogram. It is interesting to note that while the X-ray selection finds objects at a wide range in redshifts and L_{IR}, each of the other methods has a narrower range and typically identifies objects at higher luminosities. The IRAC color selection finds two peaks in the redshift distribution, one at $z \sim 0.35$ and the other at $z \sim 1.15$. For the radio, IRAC, and power-law selections the X-ray seems to detect objects over the full range of redshifts and L_{IR}. The majority of the power-law objects are ULIRGs or HyLIRGs with only a few ($\sim$10) with LIRG luminosities.

6. SUMMARY

We have presented a large robust sample of 1503 unconfused 70 μm selected galaxies with S/N > 3 (approximate flux limit of 6.5 mJy) from the 1.8 deg^2 ACS-COSMOS field. These sources span a redshift range of $0.01 < z < 3.5$ with
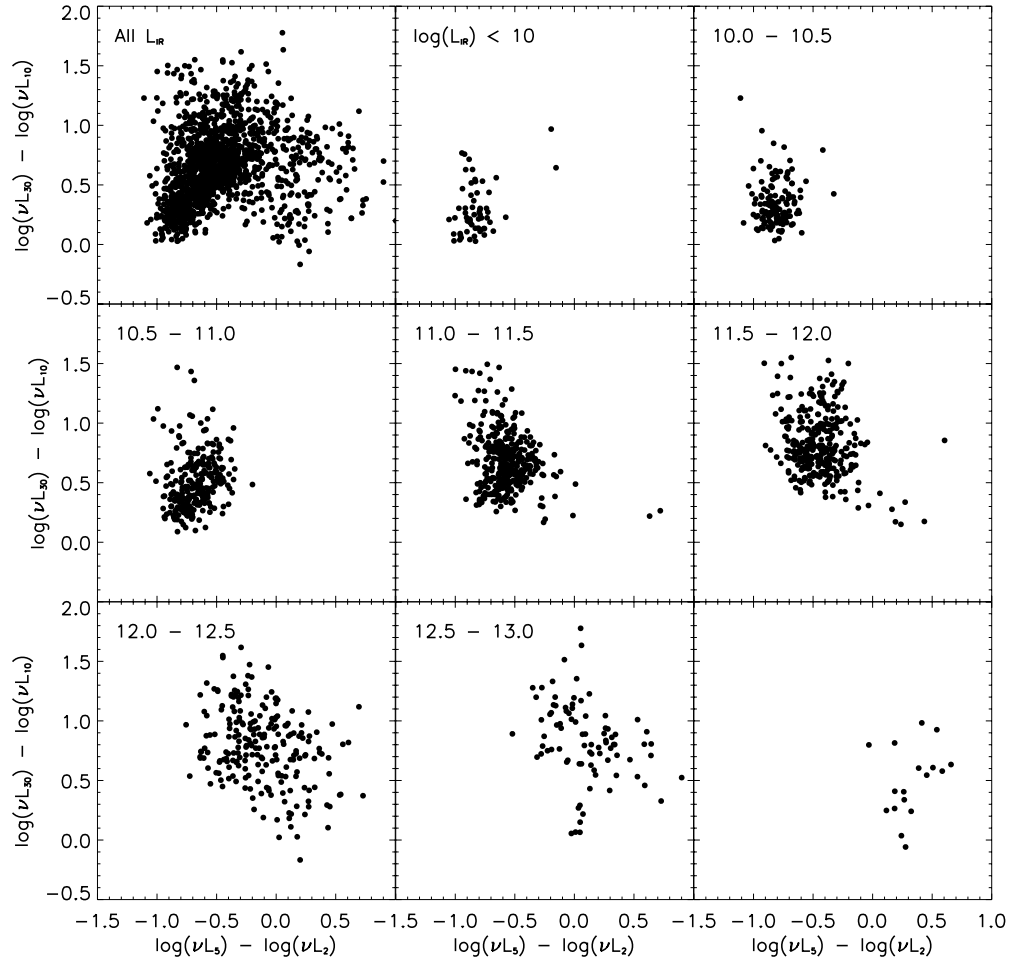
**Figure 24.** Rest-frame MIR spectral index (α_{10}^{30}) vs. NIR spectral index (α_2^5) divided into L_{IR} bins. Note that at higher luminosities ($L_{IR} > 10^{11}\,L_\odot$) a second branch appears with large values of α_2^5 (power-law SEDs) and intermediate values of α_{10}^{30}.
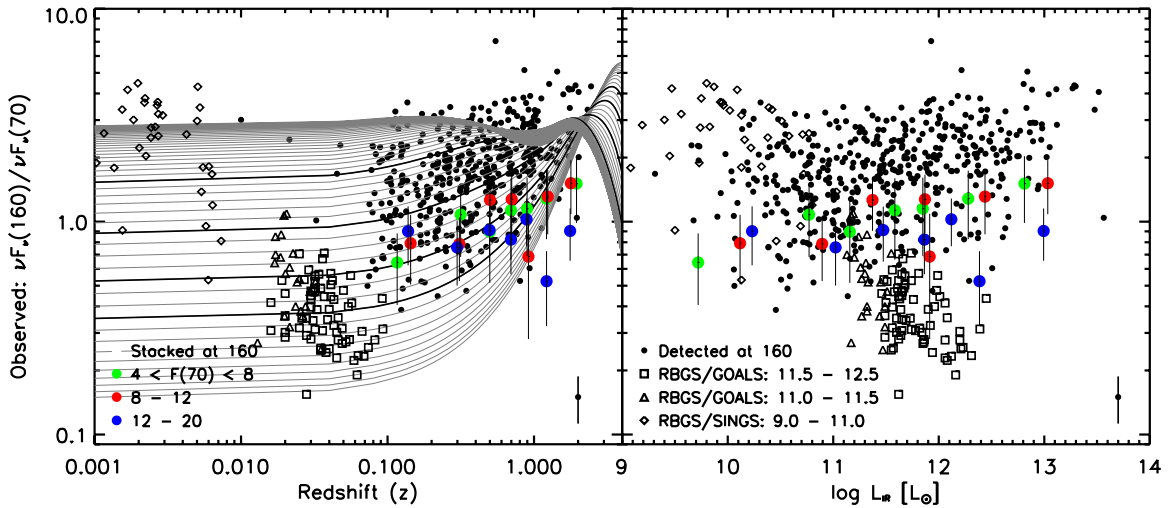

Figure 25. Observed FIR colors ($\nu F_\nu(160)/\nu F_\nu(70)$) as a function of redshift (left) and L_{IR} (right). A typical 1σ error bar is shown in the corner. The colored points represent the stacked data points (described in Section 4.4) for those sources not detected at 160 μm divided into several flux and redshift bins. Local infrared sources from the RBGS are overplotted with their FIR colors obtained from MIPS observations from SINGS ($10^9\,L_\odot < L_{IR} < 10^{11}\,L_\odot$: open diamonds) and GOALS ($10^{11}\,L_\odot < L_{IR} < 10^{11.5}\,L_\odot$: open triangles; $10^{11.5}\,L_\odot < L_{IR} < 10^{12.5}\,L_\odot$: open squares). The gray lines represent the redshift evolution of empirical templates of local objects from Dale & Helou (2002) in the luminosity range $10^{8.3} < L_{IR} < 10^{13.5}\,L_\odot$, while the black lines highlight the luminosities at 10^9, 10^{10}, 10^{11}, and $10^{12}\,L_\odot$ from top to bottom.

a median redshift of 0.5 and an infrared luminosity range of $10^8\,L_\odot < L_{IR} < 10^{14}\,L_\odot$ with a median luminosity of $10^{11.4}\,L_\odot$. This is the largest sample of 70 μm sources to date. The large multiwavelength data set available for the full COSMOS field has allowed us to compile the complete SEDs for each object from the UV to the FIR and obtain an estimate
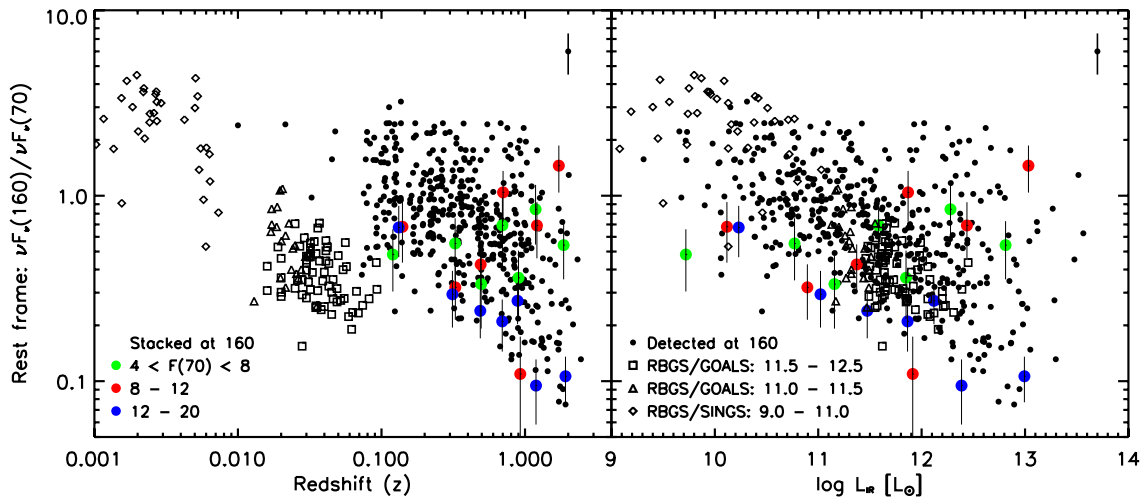
Figure 26. Same as Figure 25 but converted into rest-frame colors using the best-fit template to the infrared. Overall, the COSMOS sources span the same range in FIR colors as the local sources, however, at high luminosities there are a number of sources with colder SEDs than would be expected based on local sources. This may be evidence for a population of sources with colder SEDs at high redshift, however, at these redshifts the 160 μm data point is not long enough to constrain the peak of the SED or to obtain a precise dust temperature. The large range in SED templates that fit these data points is indicated by the fact that these sources are the same ones with a large scatter in Figure 17.
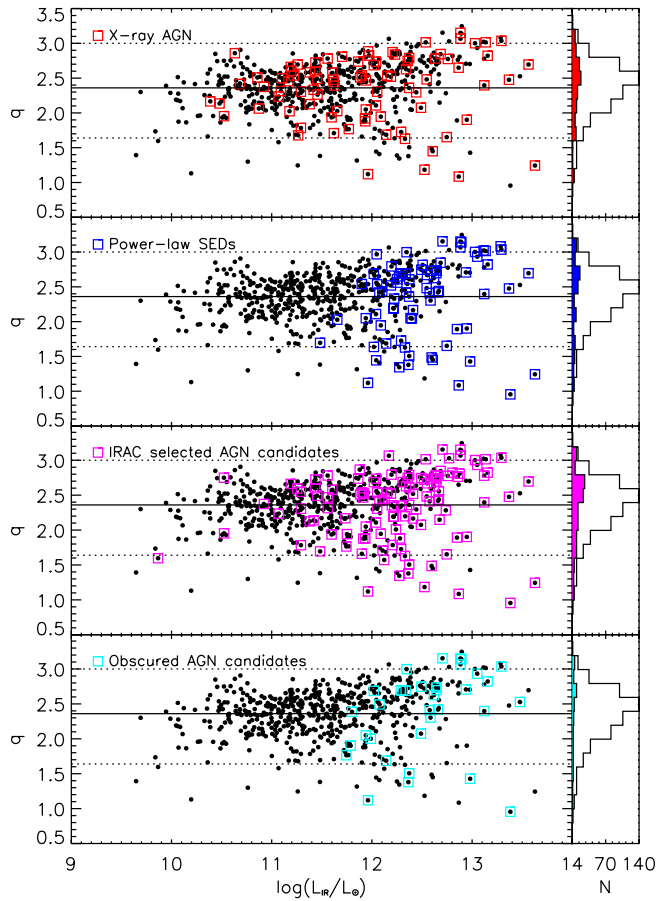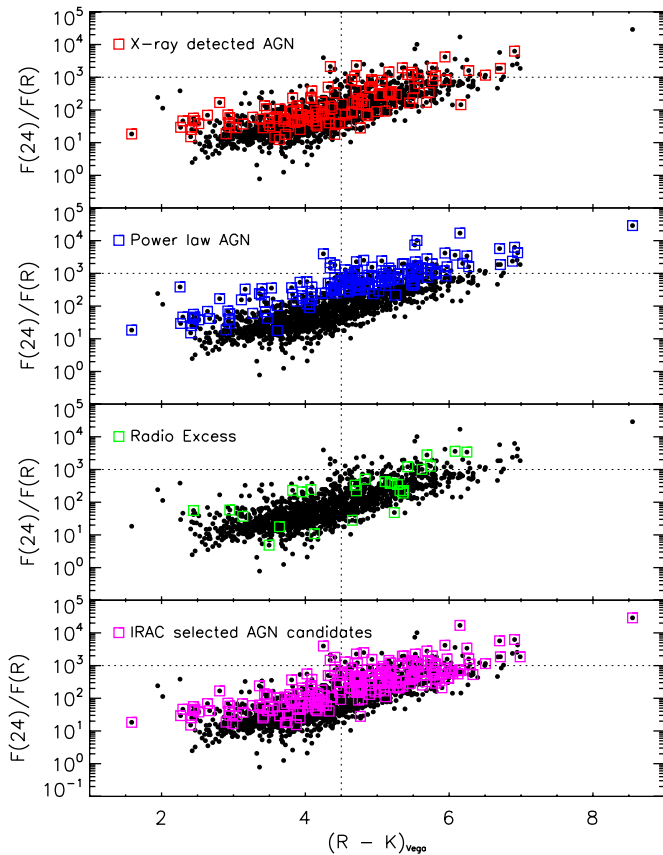

Figure 27. Radio/infrared flux ratio (q) vs. L_{IR} (same as Figure 10) with X-ray detected AGNs (red), objects with power-law SEDs (blue), IRAC color selected AGN candidates (magenta), and obscured AGN candidates (cyan) overplotted from top to bottom. The solid line indicates the median value of q (2.34) for the entire sample and the dotted lines represent the dividing lines for radio- ($q < 1.64$) and infrared-excess ($q > 3.0$) sources following Yun et al. (2001). The panels on the right show the distribution of the entire sample with radio detections and the different AGN selections overplotted in color.
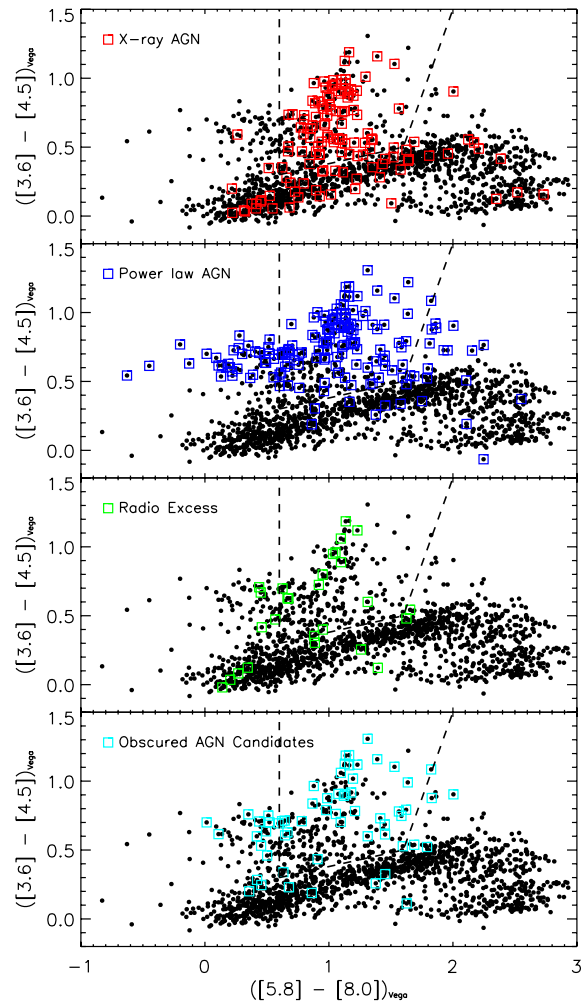

Figure 28. Stern et al. (2005) IRAC color–color plot for selecting AGN candidates with X-ray detected AGNs (red), objects with power-law SEDs (blue), radio-excess objects (green), and obscured AGN candidates (cyan) overplotted from top to bottom. The Stern et al. (2005) selection box is represented by the dashed lines.

of the total infrared luminosity. Spectroscopic redshifts are available for ∼ 40% of the sample and for the remainder we use photometric redshifts with a precision of $0.02 \times (1 + z)$. The

coverage in the X-ray, radio, and IRAC bands have allowed us to identify a large sample of potential AGNs. From the analysis of

Figure 29. MIR (24 μm) to optical (R band) flux ratio as a function of $R - K$ color with X-ray detected AGNs (red), objects with power-law SEDs (blue), radio-excess objects (green), and IRAC color selected AGN candidates (magenta) overplotted from top to bottom. The dotted lines represent the $F(24)/F(R) > 10^3$ and $R - K > 4.5$ selection cuts from Fiore et al. (2008) for obscured AGN candidates.
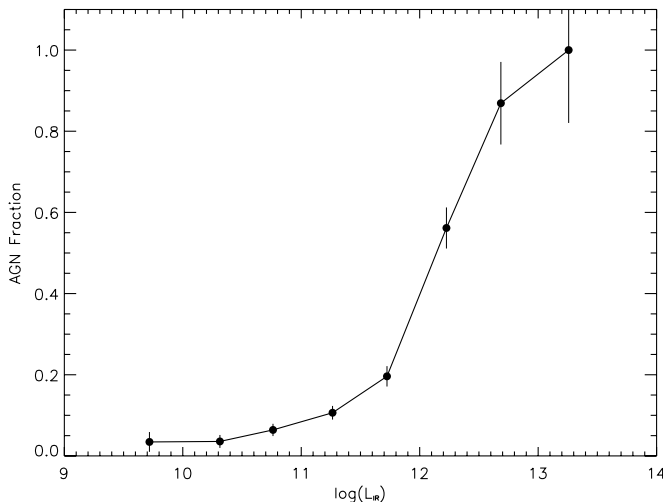
Figure 30. Fraction of 70 μm sources selected as AGN candidates by any one of the five different selection methods illustrated in Figures 27–29 as given in Column 9 of Table 6. 1σ Poissonian error bars are shown. Many of these sources are selected by more than one method though each source is counted only once. The fraction goes from < 5% at $L_{IR} < 10^{11}\,L_{\odot}$ to 100% at $L_{IR} > 10^{13}\,L_{\odot}$.

the multiwavelength properties of these objects, the following conclusions can be drawn.

1. The long-wavelength *Spitzer*-MIPS 70 and 160 μm data are essential for obtaining a more accurate and reliable estimate of the total infrared luminosity than was previously possible
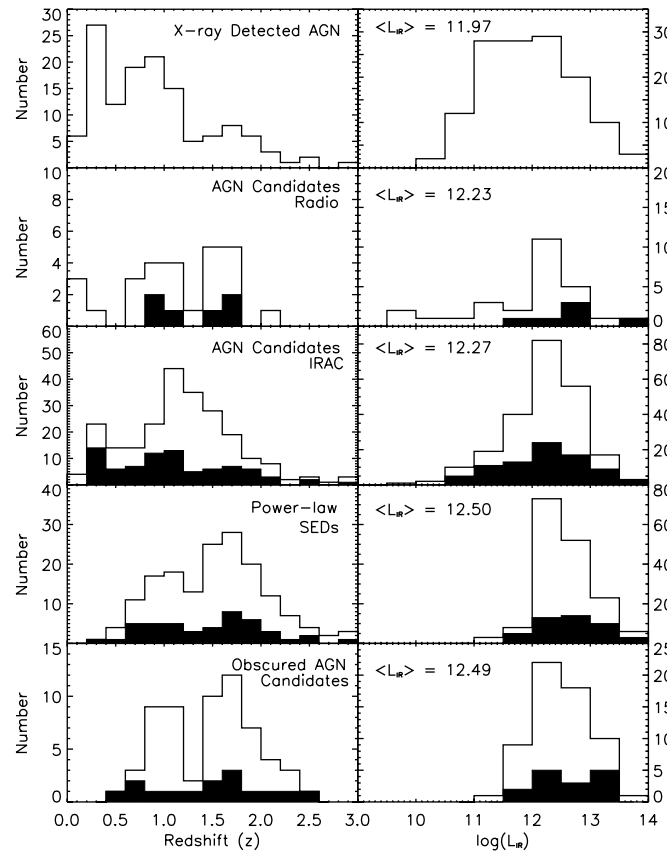
Figure 31. Redshift (left) and infrared luminosity (right) histograms for AGNs selected by each of the five different selection methods: (from top to bottom) X-ray selected, radio-excess sources, IRAC color selected sources, sources with power-law SEDs, and obscured AGN candidates. The filled histograms represent the objects in each method that are also detected in the X-ray. The median L_{IR} is plotted for each method.

using 24 μm data alone. The typical uncertainty in L_{IR} when 160 μm is detected is ~ 0.05 dex, while when it is not detected it is ~ 0.2 dex. Using only the 24 μm data point, we find the dispersion is significantly increased to ~ 0.5 dex.

2. The shape of the mean SED for the 70 μm selected sample including 18 different bands from the FUV through the FIR is similar to what has been observed for local LIRGs and ULIRGs. In particular, the maximum IR to optical ratio (~ 100) and the maximum L_{IR} ($\sim 10^{14}\,L_{\odot}$) is the same as seen locally. Our large sample presents a more complete picture of the range of SED shapes, particularly in the UV where the ratio of the optical (0.5 μm) to UV (0.2 μm) luminosities varies by nearly a factor of 1000. Similarly, the ratio of luminosities in the NIR (2–5 μm) and MIR (10–30 μm) varies by more than a factor of 100. Although our selection at 70 μm is biased toward a warmer sample at higher redshift, it still appears that the dispersion of shapes is similar at all redshifts. Clearly, one needs to consider a wider range of spectral templates as opposed to the typical cold (e.g., Arp 220) and warm (e.g., Mrk 231) templates used to represent infrared galaxies.

3. A comparison of our luminosity estimates using model fits with and without the 160 μm data points indicates that the sources detected at 160 μm have a colder SED than those not detected. This is confirmed by the difference in the FIR colors between the two subsamples. A comparison

Table 5
Fraction of 70 μm Sources Detected in the X-ray

$\log(L_{IR}/L_\odot)$	Median Redshift	Number	X-ray: Full Area[a] No. (%)	X-ray: *Chandra* Area[b] No. (%)	X-ray: *Chandra* Deep Area[c] No. (%)
< 9.0	0.02	3	0	0	0
9.0–10.0	0.10	58	3 (5.2)	1 (3.6)	0
10.0–10.5	0.17	140	8 (5.7)	4 (5.2)	2 (4.9)
10.5–11.0	0.27	281	18 (6.4)	14 (8.0)	9 (9.6)
11.0–11.5	0.47	376	35 (9.3)	27 (12.0)	15 (13.6)
11.5–12.0	0.77	311	28 (9.0)	27 (14.1)	14 (14.7)
12.0–12.5	1.05	219	29 (13.2)	19 (13.0)	14 (16.3)
12.5–13.0	1.47	84	20 (23.8)	13 (29.5)	9 (34.6)
> 13.0	2.00	31	13 (41.9)	6 (46.2)	3 (42.9)
All L_{IR}	0.50	1503	154 (10.2)	111 (12.3)	66 (14.0)

Notes.
[a] Percentage of 70 μm sources detected in the X-ray by *XMM-Newton* and *Chandra* over the full ACS area of the COSMOS field. The *XMM-Newton* observations cover 100% of this area.
[b] Percentage of 70 μm sources detected in the X-ray by *XMM-Newton* and *Chandra* in the area of the field observed by *Chandra* (55% of the ACS area) as illustrated in Figure 7.
[c] Percentage of 70 μm sources detected in the X-ray by *XMM-Newton* and *Chandra* in the area of the field with deep *Chandra* coverage (30% of the ACS area).

Table 6
AGN Fraction by Luminosity Bin

$\log(L_{IR}/L_\odot)$	Median Redshift	Number	X-ray AGN[a] No. (%)	PL[b] No. (%)	IRAC[c] No. (%)	Obscured[d] Candidates	Radio Excess[e] No. (%)	Total[f] No. (%)
< 9	0.02	3	0	0	1 (33)	0	0	1 (33)
9.0–10.0	0.10	58	0	0	1 (1.7)	0	2 (3.4)	2 (3.4)
10.0–10.5	0.17	140	2 (1.4)	0	2 (1.4)	0	1 (0.7)	5 (3.6)
10.5–11.0	0.27	281	12 (4.3)	0	10 (3.6)	0	1 (0.4)	18 (6.4)
11.0–11.5	0.47	376	28 (7.4)	3 (0.8)	19 (5.1)	1 (0.3)	3 (0.8)	40 (10.6)
11.5–12.0	0.77	311	28 (9.0)	8 (2.6)	40 (12.9)	9 (2.9)	2 (0.6)	61 (19.6)
12.0–12.5	1.05	219	29 (13.2)	73 (33.3)	82 (37.4)	22 (10.0)	11 (5.0)	123 (56.2)
12.5–13.0	1.47	84	20 (23.8)	52 (61.9)	56 (66.7)	18 (21.4)	5 (6.0)	73 (86.9)
> 13.0	2.00	31	13 (41.9)	30 (96.8)	21 (67.7)	11 (35.5)	2 (6.5)	31 (100.0)
All L_{IR}	0.50	1503	132 (8.8)	166 (11.0)	232 (15.4)	61 (4.1))	27 (1.8)	354 (23.6)

Notes.
[a] Number and percentage of objects that are detected as AGN in the X-ray (see Section 5.2 for details).
[b] Number and percentage of objects that have power-law SEDs as defined in Section 5.2.
[c] Number and percentage of objects whose colors match the AGN candidate criteria of Stern et al. (2005).
[d] Number and percentage of objects whose infrared-to-optical flux ratios ($F(24\,\mu$m$)/F(R) > 10^3$) match the Fiore et al. (2008) criteria of potentially obscured AGN.
[e] Number and percentage of objects with a radio excess (five times more radio flux than expected from the radio–IR correlation).
[f] Total number and percentage of objects that fall into any of the AGN candidate categories.

with local infrared selected sources finds the same range in FIR colors overall but also presents evidence that high-redshift and high-luminosity sources detected at 160 μm in our sample are colder than local sources of comparable luminosity. This is likely a combination of a selection effect due to the longer wavelength 160 μm detection and the poor constraints that 160 μm places on the peak of emission and dust temperature at these redshifts ($z > 1.5$). Future FIR and submillimeter studies with *Herschel* and SCUBA2 will be necessary to disentangle these possible causes.

4. We use five of the most commonly used multiwavelength selection techniques to identify potential AGNs in our sample, including 132 X-ray detected AGNs, 27 sources with radio fluxes more than five times greater than that expected from the infrared–radio correlation, 166 sources with power-law SEDs, 232 IRAC color selected galaxies, and 61 potentially obscured ($F(24\,\mu$m$)/F(R) > 10^3$) AGNs. We find that there is significant overlap among these

different methods resulting in a total of 354 sources with signatures of an AGN.

5. We find that the total fraction of AGNs increases strongly with L_{IR} similarly to the behavior of galaxies in the local universe. Our estimate indicates that nearly 70% of 70 μm selected ULIRGs and all HyLIRGs contain a powerful AGN. Less than half of the candidate AGNs selected based on several different methods are detected in the X-ray providing evidence for a significant population of obscured AGNs among this infrared selected sample. Since a 70 μm selection selects warmer SEDs at higher redshifts, it remains to be seen whether this AGN fraction is representative of all ULIRGs at these redshifts.

The complete 70 μm selected catalog of all 1503 sources including their coordinates, redshifts, and total infrared luminosities (Table 3) will be made publicly available with the online version of this paper.

REFERENCES

Abazajian, K. N., et al. 2009, ApJS, 182, 543
Alonso-Herrero, A., et al. 2006, ApJ, 640, 167
Anguita, T., et al. 2009, A&A, 507, 35
Appleton, P. N., et al. 2004, ApJS, 154, 147
Armus, L., et al. 2009, PASP, 121, 559
Bavouzet, N., Dole, H., Le Floc'h, E., Caputi, K. I., Lagache, G., & Kochanek, C. S. 2008, A&A, 479, 83
Bertin, E. 2006, in ASP Conf. Ser. 351, Astronomical Data Analysis Software and Systems XV, ed. C. Gabriel et al. (San Francisco, CA: ASP), 112
Bertin, E., & Arnouts, S. 1996, A&AS, 117, 393
Bertin, E., Mellier, Y., Radovich, M., Missonnier, G., Didelon, P., & Morin, B. 2002, in ASP Conf. Ser. 281, Astronomical Data Analysis Software and Systems XI, ed. D. A. Bohlender, D. Durand, & T. H. Handley (San Francisco, CA: ASP), 228
Bondi, M., Ciliegi, P., Schinnerer, E., Smolčić, V., Jahnke, K., Carilli, C., & Zamorani, G. 2008, ApJ, 681, 1129
Brauher, J. 2003, ESASP, 511, 21
Brusa, M., et al. 2009, ApJ, 693, 8
Cappelluti, N., et al. 2009, A&A, 497, 635
Caputi, K. I., et al. 2007, ApJ, 660, 97
Chary, R., & Elbaz, D. 2001, ApJ, 556, 562
Coleman, G. D., Wu, C.-C., & Weedman, D. W. 1980, ApJS, 43, 393
Colless, M., et al. 2001, MNRAS, 328, 1039
Condon, J. J. 1992, ARA&A, 30, 575
Condon, J. J., Anderson, M. L., & Helou, G. 1991a, ApJ, 376, 95
Condon, J. J., Huang, Z.-P., Yin, Q. F., & Thuan, T. X. 1991b, ApJ, 378, 65
Dale, D. A., & Helou, G. 2002, ApJ, 576, 159
Dale, D. A., Helou, G., Contursi, A., Silbermann, N. A., & Kolhatkar, S. 2001, ApJ, 549, 215
Dale, D. A., et al. 2007, ApJ, 655, 863
Desert, F.-X., Boulanger, F., & Puget, J. L. 1990, A&A, 237, 215
Dey, A., et al. 2008, ApJ, 677, 943
Donley, J. L., Rieke, G. H., Pérez-González, P. G., & Barro, G. 2008, ApJ, 687, 111
Donley, J. L., Rieke, G. H., Pérez-González, P. G., Rigby, J. R., & Alonso-Herrero, A. 2007, ApJ, 660, 167
Dunne, L., & Eales, S. A. 2001, MNRAS, 327, 697
Dunne, L., Eales, S., Edmunds, M., Ivison, R., Alexander, P., & Clements, D. L. 2000, MNRAS, 315, 115
Elvis, M., et al. 1994, ApJS, 95, 1

Elvis, M., et al. 2009, ApJS, 184, 158
Fiore, F., et al. 2008, ApJ, 672, 94
Fiore, F., et al. 2009, ApJ, 693, 447
Frayer, D., et al. 2006, ApJ, 647, L9
Frayer, D. T., et al. 2009, AJ, 138, 1261
Hasinger, G., et al. 2007, ApJS, 172, 29
Helou, G., Soifer, B. T., & Rowan-Robinson, M. 1985, ApJ, 298, L7
Houck, J. R., et al. 2005, ApJ, 622, L105
Huynh, M. T., Frayer, D. T., Mobasher, B., Dickinson, M., Chary, R.-R., & Morrison, G. 2007, ApJ, 667, L9
Ibar, E., et al. 2008, MNRAS, 386, 953
Ilbert, O., et al. 2009, ApJ, 690, 1236
Kennicutt, R. C., et al. 2003, PASP, 115, 928
Kim, D.-C., & Sanders, D. B. 1998, ApJS, 119, 41
Koekemoer, A. M., et al. 2007, ApJS, 172, 196
Kovács, A., Chapman, S. C., Dowell, C. D., Blain, A. W., Ivison, R. J., Smail, I., & Phillips, T. G. 2006, ApJ, 650, 592
Krugel, E. 2003, The Physics of Interstellar Dust (Bristol: Institute of Physics Publishing)
Lacy, M., et al. 2004, ApJS, 154, 166
Lagache, G., Dole, H., & Puget, J.-L. 2003, MNRAS, 338, 555
Le Fèvre, O. L., et al. 2003, Proc. SPIE, 4841, 1670
Le Floc'h, E., et al. 2005, ApJ, 632, 169
Le Floc'h, E., et al. 2009, ApJ, 703, 222
Lilly, S. J., et al. 2007, ApJS, 172, 70
Maffei, B. 1994, PhD Thesis, Institut d'Astrophysique Spatiale
Magnelli, B., Elbaz, D., Chary, R. R., Dickinson, M., Borgne, D. L., Frayer, D. T., & Willmer, C. N. A. 2009, A&A, 496, 57
Makovoz, D., & Khan, I. 2005, in ASP Conf. Ser. 347, Astronomical Data Analysis Software and Systems XIV, ed. P. Shopbell, M. Britton, & R. Ebert (San Francisco, CA: ASP), 81
Malkan, M. A., & Sargent, W. L. W. 1982, ApJ, 254, 22
McCracken, H. J., et al. 2009, ApJ, submitted (arXiv:0910.2705)
Polletta, M., et al. 2006, ApJ, 642, 673
Prescott, M. K. M., Impey, C. D., Cool, R. J., & Scoville, N. Z. 2006, ApJ, 644, 100
Sajina, A., et al. 2008, ApJ, 683, 659
Salvato, M., et al. 2009, ApJ, 690, 1250
Sanders, D. B., Mazzarella, J. M., Kim, D.-C., Surace, J. A., & Soifer, B. T. 2003, AJ, 126, 1607
Sanders, D. B., & Mirabel, I. F. 1996, ARA&A, 34, 749
Sanders, D. B., Phinney, E. S., Neugebauer, G., Soifer, B. T., & Matthews, K. 1989, ApJ, 347, 29
Sanders, D. B., et al. 2007, ApJS, 172, 86
Sargent, M., et al. 2009, ApJS, submitted
Schinnerer, E., et al. 2007, ApJS, 172, 46
Scoville, N., et al. 2007a, ApJS, 172, 38
Scoville, N., et al. 2007b, ApJS, 172, 1
Siebenmorgen, R., & Krügel, E. 2007, A&A, 461, 445
Silva, L., Granato, G. L., Bressan, A., & Danese, L. 1998, ApJ, 509, 103
Soifer, B. T., Boehmer, L., Neugebauer, G., & Sanders, D. B. 1989, AJ, 98, 766
Stern, D., et al. 2005, ApJ, 631, 163
Stetson, P. B. 1987, PASP, 99, 191
Stickel, M., et al. 2000, A&A, 359, 865
Symeonidis, M., Page, M. J., Seymour, N., Dwelly, T., Coppin, K., McHardy, I., Rieke, G. H., & Huynh, M. 2009, MNRAS, 397, 1728
Symeonidis, M., Willner, S. P., Rigopoulou, D., Huang, J.-S., Fazio, G. G., & Jarvis, M. J. 2008, MNRAS, 385, 1015
Tran, Q. D., et al. 2001, ApJ, 552, 527
Trump, J. R., et al. 2007, ApJS, 172, 383
Trump, J. R., et al. 2009, ApJ, 696, 1195
Veilleux, S., Kim, D.-C., & Sanders, D. B. 1999, ApJ, 522, 113
Veilleux, S., Kim, D.-C., Sanders, D. B., Mazzarella, J. M., & Soifer, B. T. 1995, ApJS, 98, 171
Weedman, D., et al. 2006, ApJ, 653, 101
Yan, L., et al. 2004, ApJS, 154, 60
Yang, M., Greve, T. R., Dowell, C. D., & Borys, C. 2007, ApJ, 660, 1198
Younger, J. D., et al. 2009, MNRAS, 394, 1685
Yun, M. S., Reddy, N. A., & Condon, J. J. 2001, ApJ, 554, 803
Zamojski, M. A., et al. 2007, ApJS, 172, 468